TITLE:

Quantitative Cytogenetics Reveals the Longitudinal Architecture of Meiotic Chromosome Axes

AUTHORS:

Alexander Woglar[1], Kei Yamaya[1], Baptiste Roelens[1], Alistair Boettiger[1], Simone Köhler[3] and Anne M Villeneuve[1,2*]

AFFILIATIONS:

[1]Department of Developmental Biology, Stanford University School of Medicine, Stanford, CA, USA

[2]Department of Genetics, Stanford University School of Medicine, Stanford, CA, USA

[3]EMBL Heidelberg, Heidelberg, Germany

*Correspondence: annev@stanford.edu

SUMMARY:

Here, we use quantitative cytogenetics in *C.* elegans to elucidate the molecular stoichiometry and longitudinal architecture of the cohesin-based meiotic chromosome axis, a structure required for most meiotic prophase-specific biology. We reveal a modular organization of the axis wherein different meiotic HORMAD proteins assemble into cohorts in defined numbers and co-organize the axis together with two functionally-distinct cohesin complexes in defined stoichiometry. Half of the REC-8-containing cohesin complexes loaded during S phase are lost concurrently with axis assembly, and the resulting axis contains single cohesion-mediating REC-8 complexes occurring with an average spacing of 1/130-200 kb, alternating with cohorts of axis-organizing COH-3/4 cohesin complexes (averaging 3 per module) that can associate with individual chromatids. The resulting axis/loop architecture yields an inherent asymmetry in genomic content between the loops formed on sister chromatids, potentially explaining essential but enigmatic aspects of meiotic recombination, such as the inter-homolog bias of DNA repair.

INTRODUCTION:

At the onset of meiotic prophase in organisms ranging from yeast to humans, newly replicated chromosomes adopt a highly specialized organization that enables diploid cells to produce haploid gametes. This reorganization involves the assembly of a discrete axial structure along the length of each conjoined sister chromatid pair, with the majority of DNA organized into loops emanating from this axis. These meiotic chromosome axes and/or their constituent components contribute to virtually all major aspects of meiotic prophase, including chromosome movement, homologous chromosome pairing, formation of DNA double strand breaks (DSBs), assembly of Synaptonemal Complex (SC) between aligned homologs, and repair of DSBs by interhomolog recombination to yield crossovers that will ensure homolog segregation. Thus, understanding the structure and function of meiotic chromosome axes is crucial for elucidating the mechanisms responsible for faithful inheritance of chromosomes during sexual reproduction.

A combination of genetic, cytological and biochemical approaches has identified the major components of meiotic chromosome axes in multiple different experimental systems. The foundation of the chromosome axis is built up by meiosis-specific cohesin complexes that are composed of a mixture of canonical subunits and meiosis-specific subunits. Most notably, meiosis-specific kleisin subunits have been identified in multiple organisms, including Rec8p in budding yeast (Klein et al., 1999)), RAD21L and REC8 in mammals (Eijpe et al., 2003; Parisi et al., 1999), and COH-3, COH-4 and REC-8 in *C. elegans* (Ishiguro, 2019; Pasierbek et al., 2001; Severson et al., 2009). At the onset of meiotic prophase, these cohesin complexes mediate by unknown mechanisms the recruitment of other meiosis-specific axis components. Some of these, including SYCP2/SYCP3 in mouse (Eijpe et al., 2000; Schalk et al., 1998) and Red1p in budding yeast (Smith and Roeder, 1997) have been designated as “axis core” proteins, as they play a role in recruitment of meiosis-specific HORMA-domain containing proteins (*e.g.* Hop1p in yeast (Hollingsworth and Byers, 1989) or HORMAD1/2 in mammals (Wojtasz et al., 2009); referred to as “HORMADs” from here on). The HORMADs share a structural organization in common with spindle-assembly checkpoint protein Mad2, which has a capacity to form complexes with other proteins through topological entrapment of peptides known as “closure motifs” by a Mad2 domain known as a “safety belt”

(Rosenberg and Corbett, 2015). Recent work has demonstrated that yeast Red1p and mammalian SYCP-2/SYCP-3 each contain a single closure motif that mediates interactions with their respective HORMAD partners; further, Red1p homo-tetramers and SYCP2/SYCP3 hetero-tetramers are capable of forming oligomeric filaments *in vitro* (West et al., 2019). In *C. elegans*, similar axis core components have not been identified, but four different HORMAD paralogs are present and constitute a hierarchical complex that builds up the meiotic chromosome axis (HTP-3, HTP-1/2 and HIM-3; (Couteau and Zetka, 2005; Goodyer et al., 2008; Martinez-Perez and Villeneuve, 2005; Martinez-Perez et al., 2008; Zetka et al., 1999). Further, biochemical and *in vivo* experiments have demonstrated that HTP-3 recruits HTP-1/2 and HIM-3 to the axis by interacting with their HORMA domains via closure motifs located in its C-terminal tail (Kim et al., 2014). Another recent study provided information regarding the relative cross-sectional positioning of cohesins and HORMADs within the context of the mature SCs of *C. elegans*, showing that HORMADs are located closer to the central region of the SC, whereas cohesin complexes are located closer to the bulk of the chromatin (Kohler et al., 2017).

While there has been substantial progress in identifying components of the meiotic chromosome axis and interactions among many of these components, much remains to be learned regarding how these proteins and interactions become organized along the length of chromosomes into a functional composite structure that mediates and coordinates key meiotic events. Ensemble/population-based measurements have identified preferential sites of association of multiple meiotic axis proteins in budding and fission yeast (Miyoshi et al., 2012; Panizza et al., 2011), but these analyses do not address how many (and which) sites are occupied at the same time on individual meiotic chromosomes and in a given individual meiocyte. Further, a recent Hi-C-based study of mouse spermatocytes suggests a lack of reproducible loop positions during mouse meiosis (Patel et al., 2019). It is also not known (either in meiotic cells or mitotically-dividing cells) how many cohesin complexes are required to locally provide sister chromatid cohesion ("single/simple ring" *vs.* "handcuff model", e.g.: see (Rankin and Dawson, 2016)), or how many cohesins and other axis forming proteins load onto a given stretch of DNA and organize a pair of sister chromatids into a linear axis with emanating

chromatin loops, as they appear in cytological preparations. Consequently, we currently lack understanding regarding how meiotic chromosome organization accomplishes certain essential tasks. For example: programmed meiotic DSBs must use the homologous chromosome rather than the sister chromatid as a repair template for recombinational repair, as it is necessary to form a crossover between homologs to provide the basis for a temporary link between the homologs that will ensure their correct segregation at the first meiotic division. An "*inter-sister block*" or "inter-*homolog bias*" favoring use of the homolog as a recombination partner is a long-known phenomenon in the meiotic recombination program and depends on chromosome axis proteins (for review see: (Zickler and Kleckner, 2015)), but how this bias is achieved is not understood on a mechanistic level. It is clear that our knowledge regarding how meiotic chromosome structures confer characteristic properties of the meiotic program would benefit from a fuller understanding of how the axis itself is organized.

Here, we report an analysis of the molecular stoichiometry and longitudinal architecture of the meiotic chromosome axis, using the well-established meiotic model organism *C. elegans*. Our work builds on and exploits a well-recognized feature of meiotic chromosomes from various model (and non-model) systems, namely that when meiotic nuclei are strongly spread out in 2D on a glass slide ("fully spread" from here on), the continuous axis configuration (observed in *in situ* preparations and under mild/partial spreading conditions) is "spaced out", and cohesins, axis core proteins and/or HORMADs can appear as linear arrays of foci visible by electron microscopy or immuno-fluorescence (*e.g.* see: (Anderson et al., 1988; Ishiguro et al., 2011; Kim et al., 2010; Smith and Roeder, 1997) and FIG1A). By combining this spreading approach with novel quantitative strategies and/or structured illumination microscopy (SIM), we reveal previously unrecognized features of meiotic chromosome organization. We demonstrate a modular organization of the chromosome axis in which different HORMAD proteins assemble into cohorts in defined numbers and co-organize the chromosome axis together with two structurally and functionally distinct cohesin complexes in defined stoichiometry. We show that half of the REC-8-containing cohesin complexes loaded during S phase are abruptly lost concurrently with loading of COH-3/4 cohesin complexes and axis assembly. Moreover, the resulting axis contains individual, cohesion-mediating, REC-8 complexes

occurring at an average spacing of 130-200 kb, interspersed with cohorts of axis-organizing COH-3/4 cohesins (an average of 3 per module). Finally, we provide evidence that the axis architecture deduced from our analysis can result in an inherent asymmetry in size, number and genomic composition between the loops formed on sister chromatids, a feature that can help to explain the inter-homolog bias of meiotic recombination. Together, our analyses provide a quantitative framework that will inform and constrain future experiments and models regarding meiotic chromosome axis organization and function. Moreover, the quantitative cytogenetic strategies applied here should be broadly applicable for investigating molecular stoichiometry in the context of other cellular structures and processes.

RESULTS and DISCUSSION:

Linear arrays of foci reflect modular arrangement of the meiotic chromosome axes:

In contrast to the more continuous appearance of HORMAD signals observed in *in situ* preparations of *C. elegans* gonads and under partial spreading conditions (which maintain the spatial-temporal organization of the gonad largely intact), we find that in fully spread *C. elegans* meiotic prophase nuclei, the chromosome axis is resolved as individual HORMAD foci, arranged like pearls on a string (Figure 1A), as observed in other organisms. The three types of HORMAD proteins that constitute the *C. elegans* meiotic chromosome axis (HTP-3, HTP-1/2, and HIM-3; (Goodyer et al., 2008; Martinez-Perez et al., 2008; Zetka et al., 1999)) colocalize together in most of these foci in early prophase nuclei when examined by Structured Illumination Microscopy (SIM, FIG1A), consistent with the demonstrated direct physical interactions among these components (Goodyer et al., 2008; Kim et al., 2014). Further, previously reported findings concerning distinct behaviors of different HORMAD proteins could be recapitulated in these fully spread preparations. For example, in late prophase, crossover designation triggers the reorganization of the *C. elegans* meiotic bivalent into two distinct domains: a long arm, where all the HORMADs are present, and a short arm, where only HTP-3 and HIM-3 are present (Martinez-Perez et al., 2008); this reorganization is clearly visible in the fully-spread preparations (FIG1A).

We count approximately 1000 HORMAD-containing foci (HIM-3 and HTP-3) in fully-spread pachytene nuclei (FIG1A, bottom right). These individual HORMAD foci are connected along a given chromosome stretch by DAPI-positive threads, the chromosome loops. For each chromosome axis, these DAPI-positive loops correspond to a pair of sister chromatids, for a total of four individual chromatids per bivalent (FIG1A).

C. elegans HORMAD protein HTP-3, which is required to load all the other HORMADs (Goodyer et al., 2008), appears to play a role in axis organization analogous to the axis core proteins (Red1 and SYCP2/SYCP3) identified in other organisms. In the absence of HTP-3, meiotic cohesin complexes still bind chromatin and hold sister chromatids together until anaphase (Severson et al., 2009), but they are not arranged as a continuous axis or in a pearls-on-a-string-like configuration during prophase (FIG1S1). Thus, absence of HTP-3 phenocopies budding yeast *red1* mutants (in which axes don't form, but cohesin binding is unaffected), rather than *hop1* mutants (in which Red1p and Rec8p containing axes form) (Klein et al., 1999; Woltering et al., 2000). Therefore, we speculate that HTP-3, which contains six closure-motifs that mediate associations with HIM-3 and HTP-1/2 (Kim et al., 2014), functions as the axis core component in *C. elegans*.

During metazoan meiosis, chromosome axis organization and meiotic sister chromatid cohesion are mediated by at least two different cohesin complexes that contain distinct kleisin subunits and/or load at distinct times. Sister chromatid cohesion is mediated by complexes containing REC-8 in worms, REC8 in mammals and C(2)M in flies, whereas axis formation requires COH-3 and COH-4 in worms, REC8 and RAD21L in mammals and the SOLO-SUNN-containing cohesin complex in flies (Crawley et al., 2016; Gyuricza et al., 2016; Pasierbek et al., 2001; Severson et al., 2009; Xu et al., 2005). Because COH-3 and COH-4 are products of a recent gene duplication, are functionally redundant and are recognized by the same antibody, they are referred to as COH-3/4 from here on (Severson et al., 2009; Severson and Meyer, 2014).

When HORMADs (*e.g.* HTP-3), COH-3/4 and REC-8 foci are visualized simultaneously in fully-spread nuclei, such foci occur in roughly the same numbers (about 1000 foci per nucleus, FIG1A). Moreover, the HORMAD, COH-3/4 and REC-8 signal peaks usually do not coincide with each other, yet they are arranged in a 1:1:1 modular fashion along a given chromosome stretch (FIG1B). If we consider the numbers of these

HORMAD/cohesin (REC-8 and COH-3/4) foci modules to be distributed along the diploid genome (2 x 100 Mbp), we can estimate an average spacing of one HORMAD/cohesin module for every ~200 kbp. Because overlap between some chromosome segments in spreads of whole nuclei might result in an underestimate of foci numbers, we sought to validate this estimate by measuring numbers of foci on well-separated DNA segments of defined size.

Our approach was to evaluate numbers of cohesin and HORMAD foci on extra-chromosomal arrays (ExChrs), which are mini-chromosomes that form via fusion of linear or circular DNA of any origin upon injection into the *C. elegans* gonad. ExChrs are visible as additional DAPI bodies in oocytes, which allows an approximation of their size (FIG1C). Depending on the mixture of injected DNAs, ExChrs can be highly repetitive or complex in DNA sequence. Repetitive ExChrs acquire heterochromatic marks and are silenced in the germ line, whereas complex ExChrs can be transcriptionally active in germ cell nuclei (Kelly et al., 1997). ExChrs can be transmitted through mitosis and can be inherited across generations, albeit in non-Mendelian fashion (Mello et al., 1991; Stinchcomb et al., 1985).

Here we analyzed ExChr *oxEx1578*, a repetitive array that has 0% *E. coli* genomic DNA, and *meEx001*, a complex array that has 95% *E. coli* genomic DNA. Based on 3D DAPI intensity measurements in diakinesis-stage oocytes, we estimate that *meEx001* contains about 1 Mbp of DNA and *oxEx1578* contains about 2.2 Mbp, corresponding to approximately 1% and 2% of the size of the *C. elegans* haploid genome, respectively (FIG1C). Interestingly, we found that ExChrs are ring chromosomes (FIG1S2A), as suggested by S.K. Kim in 1992 (http://wbg.wormbook.org/wli/wbg12.2p22). Both *meEx001* and *oxEx1578* form chromosome axes during meiotic prophase, but do not engage in synapsis when more than one ExChr is present in the nucleus (FIG1S2A).

In fully spread nuclei, we find that ExChrs are decorated by HTP-3, COH-3/4 and REC-8 foci in a pattern similar to that observed on normal chromosomes (FIG1C). Numbers of HORMAD foci and cohesin foci on a given ExChr are strongly correlated (FIG1S2B), consistent with the modular organization described above. Further, the average numbers of foci observed for these two ExChrs were proportional to the amount of DNA present, as we detected twice the number of foci on the ExChr that contains twice

the amount of DNA (*meEx001*: HTP-3: 7.8(+/-2.4), REC-8: 8.1(+/-2.5) and COH-3/4: 7.8(+/-2.6) foci; *oxEx1578*: HTP-3: 16.1(+/-2.9), REC-8: 16.8(+/-2.8) and COH-3/4: 15.3(+/-3.1) foci, FIG1C and FIG1S2B).

Our observation that *meEx001* and *oxEx1578* exhibit the same average densities of cohesin and HORMAD foci is remarkable given that these two ExChrs share almost no sequences in common with each other or with the *C. elegans* genome (except for a promoter fragment and plasmid sequences in the selection markers that are present in vastly different amounts in the two ExChrs). Moreover, *meEx001* is a young chromosome (analyzed in generations 4-9 after its creation) and had not yet reliably acquired heterochromatic marks (only 5/25 rings analyzed were enriched for H3K9me2), whereas *oxEx1578* was generated years ago in the Jorgensen lab (Frokjaer-Jensen et al., 2012), has been maintained for many generations, and is strongly heterochromatic in the germline (25/25 rings were enriched for H3K9me2, FIG1S2B). Thus, we conclude that HORMAD/cohesin modules occur along chromosomal DNA with an average spacing of approximately 130-200 kbp, and that they can do so apparently independently of DNA sequence or epigenetic state.

Inferring the numbers and stoichiometry of cohesin and HORMAD molecules in chromosome axis foci:

Next, we set out to determine the numbers of the different cohesion and HORMAD proteins present in the individual axis foci that we observe cytologically.

First, we present evidence indicating that individual REC-8 foci detected in fully-spread nuclei each represent a single REC-8 cohesin complex: We examined chromosome axes in fully-spread meiotic chromosomes from worms expressing two differently-tagged versions of REC-8 (REC-8::3xFLAG and REC-8::GFP) in the same animal; no untagged REC-8 was expressed in these worms. If REC-8 foci represented cohorts of multiple REC-8 cohesin complexes, we would have expected to observe frequent colocalization of the two tags. Instead, visualization by immuno-fluorescence and SIM imaging revealed that both tagged proteins are integrated into the chromosome axes, but they do not colocalize (FIG2A). Importantly, the same result was obtained when detection of FLAG and GFP was performed sequentially, in either order, ruling out the

possibility that lack of colocalization of the two tags might have been caused by antibody exclusion (FIG2A and FIG2fS1A). Thus, we conclude that each single REC-8 focus in the fully-spread preparations represents a single cohesin complex.

Having established that single cytological REC-8 foci represent single REC-8 molecules, we set out to deduce the numbers and relative stoichiometry of other cohesin subunits and different HORMAD components associated with meiotic chromosome axes using quantitative analysis of wide-field immuno-fluorescence images.

We used two different independent approaches to infer the relative numbers of REC-8 and COH-3/4 containing cohesin complexes. First, we measured and compared the total amount of chromatin-bound SMC-1 (which is present in all cohesion complexes) and chromatin bound REC-8. Nuclei from gonads of two distinct genotypes, one expressing REC-8::FLAG (identified by GFP::COSA-1 expression) and the other expressing SMC-1::FLAG (identified by mEos::HIM-3 expression) were spread together on the same glass slide, immuno-stained for the Flag epitope and HIM-3, and imaged using the same conditions (FIG2B). Whereas anti-HIM-3 and DAPI fluorescence were not distinguishable between the two genotypes (FIG2B and data not shown), the average total FLAG immuno-fluorescence signal for the nuclei expressing SMC-1::FLAG was 4 times that for the nuclei expressing REC-8::FLAG. Thus, we estimated there to be 4 times more chromatin/DNA bound SMC-1 than REC-8 molecules. We corroborated and extended this finding using an orthogonal approach in which we visualized and measured SMC-1 fluorescence signals (visualized with an HA tag) in 800nm x 800nm ROIs encompassing individual SMC-1 foci (FIG2C). SMC-1 fluorescence values were compared for three classes of foci, *i.e.*, those associated with: a) COH-3/4 but not REC-8; b) both COH-3/4 and REC-8; c) REC-8 but not COH-3/4. The average SMC-1::HA fluorescence measured for “COH-3/4 only” foci was 2.8 x that measured for “REC-8 only” foci, and the average SMC-1::HA fluorescence for SMC-1 foci associated with both COH-3/4 and REC-8 was 4 x that for “REC-8 only” foci. Further, the total fluorescence measurements for COH-3/4 and for SMC-1 within the same foci are highly correlated (FIG2S1B), reinforcing the idea that REC-8 and COH-3/4 are the major, and possibly only, kleisins present in chromatin-bound cohesin complexes during meiosis (Severson et al., 2009). In summary, our two different quantification approaches together revealed

that the individual HORMAD/cohesin modules that make up the axis contain, on average, four cohesin complexes: one containing REC-8 and three containing COH-3/4.

We also wished to determine the number and relative stoichiometry of different HORMAD components in the chromosome axis foci. To this end, we made pairwise comparisons of relative fluorescence intensities of foci for different axis components marked with the same tag, using HTP-3 as a standard for aligning the different comparisons. For each of these experiments, we isolated nuclei from two different genotypes (one expressing 3xFLAG::HTP-3::GFP and one expressing REC-8::GFP, GFP::HIM-3, or HTP-1::GFP), then mixed and spread them together on the same slide, and stained and imaged them using the same conditions. For the data in FIG2D, we measured fluorescence within 400x400 nm ROIs encompassing well-isolated individual foci and normalized our data to the mean fluorescence intensity measured for REC-8 foci, as we consider these to represent single molecules. Using this approach, we estimated that a single cytological HORMAD focus contains, on average, 2.9 (+/-0.68) HTP-3 molecules, 5.1 (+/-2) HTP-1 molecules, and 7.8 (+/-2.9) HIM-3 molecules (FIG2D). The relative ratio of GFP::HIM-3 to HTP-3::GFP calculated using this approach (2.7 : 1) is in good agreement with that estimated using a different method that evaluates total fluorescence in partially spread nuclei (3.2 : 1) (FIG2S2A).

HORMAD proteins HTP-1 and HTP-2 are nearly identical, and although HTP-2 is largely dispensable for successful meiosis, they do have partially overlapping functions (Couteau and Zetka, 2005; Martinez-Perez et al., 2008; Martinez-Perez and Villeneuve, 2005). Thus, the value calculated for HTP-1::GFP is expected to be an underestimate of the total number of HTP-1/2 molecules associated with meiotic chromosome axes in nuclei that contain a mixture of tagged HTP-1 and untagged HTP-2. Indeed, we found that the ratio of HTP-1::GFP to GFP::HIM-3 was significantly higher for nuclei that lacked HTP-2 (1.9 : 1) than for nuclei where HTP-2 was present (1.4 : 1) (FIG2S2B). Thus, we infer that a single HORMAD focus most likely contains an average of 6 HTP-1/2 molecules during WT prophase.

The wide ranges of fluorescence values measured for HTP-1 and HIM-3 foci likely reflect biological variation in the numbers of HTP-1 or HIM-3 molecules present in different HORMAD modules, as we find that HTP-1/2 and HIM-3 protein levels in meiotic

nuclei increase over the course of meiotic prophase (FIG 2S2C). In contrast, HTP-3 levels remain largely stable from meiotic entry through the end of pachytene (FIG 2S2C). Overall, our data are in strong agreement with biochemical and structural data from a recent study that investigated interactions among *C. elegans* HORMAD proteins (Kim et al., 2014). This study found that the HIM-3 HORMA domain can bind to 4 of the 6 closure motifs in the C-terminal tail of HTP-3, and the HORMA domains of HTP-1/2 can bind to the remaining two motifs. Moreover, when the proteins are co-expressed in bacteria, HTP-3 and HIM-3 form complexes in a 1:2 or 1:3 ratio, while HTP-3 and HTP-1 do so in a 1:2 ratio. Thus, our data quantifying the numbers of foci per nucleus and their relative fluorescence are consistent with a model in which meiotic chromosome axes are assembled from interactions between individual modules that are each composed of cohesin and HORMAD proteins in the following stoichiometry: [1 REC-8 cohesin] : [3 COH-3/4 cohesins] : [3 HTP-3 : 6-9 HIM-3 : 6 HTP-1/2], distributed along chromosomes with an average density of 1 module for every 130-200 Kb.

Non-random arrangement of structurally and functionally distinct cohesin complexes along chromosome axes:

Previous work provided evidence that REC-8 and COH-3/4 cohesin complexes play functionally distinct roles during *C. elegans* meiosis (Severson et al., 2009; Severson and Meyer, 2014): REC-8 has been demonstrated to mediate sister chromatid cohesion, whereas COH-3/4 plays a key role in axis organization (FIG3S1A). Further, these functionally distinct complexes differ in their timing of association with chromatin: REC-8 cohesins (like murine REC8) load during pre-meiotic DNA replication, whereas COH-3/4 cohesins (like murine RAD21L) load after completion of S phase, at the beginning of prophase ((for review: (Ishiguro, 2019)). Our data support and extend these findings in several ways.

First, measurement of fluorescence levels in immuno-stained gonads demonstrated that half of the REC-8 cohesin complexes loaded during S phase are removed from chromatin concurrently with loading of COH-3/4 cohesin complexes and coalescence of meiotic chromosome axes (FIG3A). This suggests that a fundamental shift in the relationships between sister chromatids may occur upon entry into meiotic

prophase. The sharp drop of REC-8 molecules upon meiotic prophase entry does not depend on the presence of COH-3/4, as it occurs even in a *coh-4 coh-3* mutant (FIG3S1B). Cohesin release factor WAPL-1 may play a role in REC-8 removal, as a drop in REC-8 levels upon meiotic entry is not observed in a *wapl-1* mutant (FIG3S1B); however, interpretation of this finding is complicated by the fact that COH-3/4 cohesins load prematurely at low levels during S phase in the *wapl-1* mutant (Crawley et al., 2016), so REC-8 may not be loaded at normal levels in this mutant.

Second, analysis of SIM images of fully spread chromosome axes revealed that not only do COH-3/4 and REC-8 signal peaks usually not coincide, but COH-3/4 and REC-8 signal peaks usually occur in a largely alternating pattern along a given axis stretch (FIG3B). This striking alternating arrangement is significantly different from simulated random positioning along a theoretical axis, strongly suggesting a functional biological basis underlying the observed pattern.

Third, analysis of spread nuclei from *rec-8* mutants provides additional evidence for a functional distinction between REC-8 and COH-3/4 cohesin complexes, by demonstrating a capacity for COH-3/4 cohesin complexes to interact with individual chromatids. In *rec-8* mutants, when only COH-3/4 cohesin complexes are present on chromatin during meiotic prophase, SCs frequently form and crossover recombination apparently occurs between sister chromatids (rather than between homologs), suggesting that axes assemble along individual chromatids in this context (Crawley et al., 2016). However, we find that not all chromosomes engage in synapsis in *rec-8* mutants, and we were able to trace the paths of both synapsed and unsynapsed axes in late prophase nuclei of *rec-8* mutants. This analysis confirmed the interpretation that continuous chromosome axes (containing HTP-3 and COH-3/4) do indeed form along individual chromatids in the *rec-8* mutant (FIG3C and FIG3S1C). Thus, we infer that while REC-8 cohesin complexes are required to confer cohesion between sister chromatids, COH-3/4 cohesin complexes are sufficient to organize axes and can topologically embrace or bind to single chromatids (rather than sister chromatid pairs), at least when REC-8 cohesin is absent.

Model for chromosome axis assembly and implications for axis/loop organization.

Based on our data, we propose the following model for the assembly of meiotic chromosomes axes: upon completion of pre-meiotic S-phase and entry into meiotic prophase, half of the REC-8-containing cohesin complexes, which were loaded during S-phase and hold sister chromatids together, are removed from chromatin. This presumably loosens the associations between sister chromatids between the positions where REC-8 cohesins are retained. Concurrently, COH-3/4-containing cohesin complexes bind and/or capture DNA from only one of the two individual sister chromatids, helping to promote the formation of loops in the intervals between the positions where REC-8 complexes are maintaining cohesion between the sister chromatids. This organization is "locked in" by binding of HORMAD proteins, resulting in a linear arrangement of HORMADS and cohesion complexes along the longitudinal axis of the chromosome (FIG4A).

COH-3/4 cohesins can bind independently to either of the two individual sister chromatids. Moreover, there are, on average, an odd number of COH-3/4 cohesin complexes (*i.e.* three) in a given interval between two REC-8 cohesion-mediating complexes. Thus, chromatin loops that form on each sister chromatid in between two REC-8 cohesion-mediating complexes could potentially be inherently different from each other in number and size, and consequently in DNA content ("asymmetric loops"). This would contrast with the usual depiction of "symmetric loops" on the two sister chromatids that are of the same size and DNA content (FIG4B).

We used an immuno-FISH (fluorescence *in situ* hybridization) approach to test whether chromosome loops associated with pairs of sister chromatids appear "symmetric", "asymmetric" or both. We labeled two consecutive 200 kbp regions of chromosome II with 2 different-colored FISH probes, and we measured the distances from the junctions between the two probes (where the two colors meet) to the chromosome axes (marked by HTP-3). If loops are symmetric, the distance between the FISH probe junction and the chromosome axis should be the same for the two sister chromatids. In contrast, if loops are asymmetric, the distances between the FISH probe junctions and the chromosome axis should differ for the two sister chromatids (FIG4B). To be able to distinguish between signals from sister chromatids and the homologous chromosome, we used worms heterozygous for an internal inversion of chromosome II (*mIn1*), which results in wide spacing between the FISH signals associated with the two

homologous chromosomes (FIG4C). For this assay, we analyzed 81 sister chromatid pairs on minimally-disrupted chromosomes prepared using partial spreading conditions (FIG4D and FIG4S1). In 32% of cases (26/81), the FISH probe junctions of the two sister chromatids were not cytologically resolvable between the two sister chromatids and thus could potentially represent either symmetric loops or asymmetric loops that were too small to be resolved. In 26% of cases (21/81) the FISH probe junctions were found at similar distances (differing by ≤400 nm) from the chromosome axes, consistent with symmetric loops. Finally, in 42% of cases (34/81), the distances between the FISH probe junctions and the chromosome axis differed by >400 nm for the two sister chromatids, presumably indicative of asymmetric loops that were large enough to be resolved by our assay (FIG4D). Thus, we conclude that the loops present on pairs of sister chromatids are frequently distinct from each other in size and/or position, and consequently, in genomic content.

Asymmetry between sister chromatid loops can potentially help to explain some important properties of the meiotic recombination program. Since the DSBs that serve as the initiating events of meiotic recombination are thought to be generated in loop regions that are tethered to the chromosome axis (Blat et al., 2002; Panizza et al., 2011), such asymmetry between sister-chromatid loops could potentially prevent DSBs from occurring at the same site on both sister chromatids during the same meiosis. Furthermore, the proposed axis-loop organization could also contribute to the inter-homolog repair bias of meiotic recombination (Haber et al., 1984; Jackson and Fink, 1985; Schwacha and Kleckner, 1994), as an intrinsic feature of the proposed configuration is that sister chromatids would almost never share the same loop domains and thus would not be favored as DNA repair partners.

The approaches employed in this work have enabled us to deduce the numbers, relative stoichiometry and spatial distribution of multiple proteins that are central to the functional organization of chromosomes during meiosis. Further, our data regarding the density of HORMAD/cohesin modules (1 per 130-200 kbp) and the stoichiometry of proteins within these modules can be used to calculate the density of cohesin complexes along *C. elegans* meiotic prophase chromosomes. Given an average of four cohesin complexes (1 REC-8 and 3 COH-3/4) in each module, we can infer that there are

approximately 20 - 30 cohesin complexes per Mb of chromosome length when each pair of sister chromatids is considered as a single conjoined entity. When considering the total amount of DNA in each sister chromatid pair, this translates to a density of 10 - 15 cohesin complexes per Mb of DNA. These measurements of cohesin density on *C. elegans* meiotic chromosomes are in remarkably close agreement with recent independent estimates of cohesin density deduced for mouse ES cells based on in-gel fluorescence measurements and fluorescence correlation spectroscopy (FCS)-calibrated imaging (5.3 complexes/Mb; (Cattoglio et al., 2019)) and for HeLa cells based on quantitative mass spectrometry and FCS-calibrated imaging (8.5-17 complexes/Mb; (Holzmann et al., 2019)), supporting both the validity of our experimental approach and the broad relevance of our findings to the field of chromosome biology. Thus, we anticipate that other features revealed in the current work, such as spatial alternation between cohesion-mediating cohesin complexes and putative axis/loop-organizing cohesin complexes, may reflect generalizable principles and properties of chromosome organization that operate in other contexts. Finally, we note that the approaches we devised here to quantify numbers and/or relative stoichiometry of chromosome axis components should be widely applicable for analyzing many other cellular structures and biological processes, enabling quantitative estimates of molecular components that can inform and constrain models regarding how such structures and processes assemble and function.

ACKNOWLEDGMENTS:

We are grateful to A. Dernburg, B. Meyer, A. Severson and E. Martinez-Perez for antibodies and strains. We thank J. Mulholland, K. Lee, A. Kahn and C. Akerib for technical assistance and discussions and A. MacQueen, E. Martinez-Perez, C. Jacovetti and C. Akerib for comments on the manuscript. This work was funded by an American Cancer Society Research Professor Award (RP-15-209-01-DDC) and NIH grants R01GM53804 and R35GM126964 to AMV, a FWF Erwin Schrödinger Fellowship (J-3676) to AW and grant 1S10OD01227601 from the NCRR to the Stanford Cell Science Imaging Facility.

AUTHOR CONTRIBUTIONS:

Investigation: AW and KY. Conceptualization, Methodology: AW. Formal Analysis, Funding Acquisition: AMV and AW. Writing - original draft: AW. Writing – review and editing, Resources: AMV, AW, KY, BR, SK and AB.

DECLARATION OF INTRESTS:

The authors declare no competing interests.

FIGURE LEGENDS:

Figure 1. **Density of chromosome axis modules.** A) TOP: Comparison of Structured Illumination Microscopy (SIM) images of *in situ*, partially spread, and fully spread individual meiotic prophase nuclei, displayed at the same magnification. In the image at the right, dashed lines outline the domains of each of the six bivalents where HTP-1/2 proteins have become depleted from the chromosome axis, indicating that this nucleus is at the late pachytene stage. BOTTOM LEFT, CENTER: Images of cropped segments of synapsed chromosome pairs, illustrating both the pearls-on-a-string appearance of chromosome axis foci and colocalization of HTP-3 and HIM-3 (overlaid) or HTP-1/2 (images offset in both x and y); range of R values from ImageJ Coloc2 analysis for 8-10 individual fully spread nuclei. BOTTOM, RIGHT: Quantification of numbers of HTP-3, HIM-3 REC-8 and COH-3/4 foci in individual fully spread nuclei; each data point represents a nucleus.

B) LEFT: Chromosome axis segments from a fully-spread prophase nucleus from a worm expressing REC-8::GFP. GFP, COH-3/4 and HTP-3 were detected by antibody staining and visualized by SIM. RIGHT: Representation of the positions of manually-identified signal intensity peaks for GFP, COH-3/4 and HTP-3 foci in the image on the left.

C) TOP: Method used to estimate the total DNA content of two distinct ExChrs, *meEx001* and *oxEx1578*. Sample deconvolved wide-field images of DAPI-stained chromosome complements from individual oocyte nuclei (with the ExChrs circled) are presented together with masks generated using the “3D Object Counter” ImageJ plugin; in the accompanying graph, each data point represents the total DAPI fluorescence for a single ExChr (2C), normalized to ½ of the total DAPI fluorescence measured for all 6

bivalents (4C) in the same nucleus. BOTTOM, LEFT and RIGHT: Individually cropped examples of ExChr *meEx001* (left) and *oxEx1578* (right) from fully-spread nuclei stained for COH-3/4 or REC-8 together with HTP-3. BOTTOM, CENTER: Table representing the average densities per Mbp of HTP-3, REC-8 and COH-3/4 foci derived from our analyses counting foci for the whole genome and for the ExChrs (see FIG1S2B and FIG1A, bottom).

Figure 1S1. **Requirement for HTP-3 in organizing cohesins into axial arrays.** Images of cohesin components SMC-1 and REC-8 and SC central region component SYP-1 in partially spread nuclei from *htp-3* mutant gonads, visualized by wide-field deconvolution microscopy. SMC-1 and REC-8 are not detected as linear arrays of foci or as continuous axes in either early or late prophase nuclei (indicated by the presence of 1-3 SYP-1 aggregates).

Figure 1S2. **Structure and features of ExChrs.** A) Circular structure of ExChrs. Left, schematic illustrating that multiple circular and/or linear DNA molecules co-injected into the *C. elegans* germ line co-assemble into extra-chromosomal arrays that can be inherited as mini-chromosomes. Right, SIM images of HTP-3-marked chromosome axes in spread nuclei carrying ExChrs, which appear as rings. Insets show multiple rings cropped from different nuclei from the same strain; the fact that rings from a given strain are similar in size indicates that once formed, ExChrs tend to be stable in size. The rings depicted are two different examples from 21 independent lines generated using the same selection scheme [*cb-unc-119(+)* in the *unc-119(ed3)* mutant], either alone or together with 10-90% *E. coli* genomic DNA (linearized by sonication and size selected to 1-5 Kb by gel extraction) in the injection mix. The transmission rates of the Unc+ trait in self-fertilizing hermaphrodites varied widely, ranging from 10-95%, and did not correlate with the percentage of *E. coli* DNA present in the injection mix. In 18 of the 21 lines, ExChrs could be detected as additional HTP-3-positive structures in meiotic prophase nuclei, and in 16 of these 18 cases, the ExChrs were reliably resolvable as rings by SIM in partially spread gonads; as the two ExChrs that were not verified as

rings were the smallest of the 18, we speculate that they may also be rings, but their small size prevented their ring structure from being resolved microscopically.

B) Density of axis components on circular ExChrs. TOP: For each of the two ExChr-bearing strains depicted, the large images on the right show portions of nuclei from partially spread gonads prepared using conditions that preserve SCs, stained for HTP-3, COH-3/4 and SYP-1. At the left, schematic representations of the DNA composition of *meEx001* and *oxEx1578* are presented together with SIM images of individual cropped ExChrs stained for HTP-3 and H3K9me2. BOTTOM: Quantification of axis foci on ExChrs in fully-spread nuclei stained for either REC-8 or COH-3/4 together with HTP-3. In the graphs, each data point represents a single ExChr, with the X-axis indicating the numbers of REC-8 or COH-3/4 foci and the Y-axis indicating the numbers of HTP-3 foci counted on that ExChr. All data acquired are presented. For both ExChrs examined, the numbers of HTP-3 and REC-8 or COH-3/4 foci are strongly correlated ($p<0.001$) and the slopes of the linear regression lines are near to 1 (for *meEx001* REC-8 vs. HTP-3, r = .85, slope = .79; for *meEx001* COH-3/4 vs. HTP-3, r = .88, slope = .84; for *oxEx1578* REC-8 vs. HTP-3, r = .94, slope = .76; for *oxEx1578* COH-3/4 vs. HTP-3, r = .76, slope = .79). Further, in three of the four cases, a line with slope = 1 falls within the 95% confidence interval for the slope of the linear regression line (indicated by the gray shaded area), consistent with a near 1:1:1 correspondence between HORMAD, REC-8 and COH-3/4 foci, as observed for spread chromosome segments depicted in FIG1. Thus, we infer that axis organization on the ExChrs is similar to that observed for normal chromosomes.

Figure 2. **Quantitation of numbers of chromosome axis proteins present in individual axis module foci.** A) Sample SIM image of a fully-spread nucleus from a worm expressing both REC-8::GFP and REC-8::3xFLAG, immuno-stained for HTP-3, FLAG and GFP; all REC-8 molecules present harbor one or the other tag. (In this case, the specimen was stained sequentially: anti-GFP was applied first, followed by secondary detection, before primary and secondary immuno-detection of HTP-3 and FLAG; also see FIG2S1A). Although GFP and FLAG signals both localize to chromosome axes (marked by HTP-3, left), they do not colocalize with each other.

Coloc2 analysis using ImageJ confirmed little to no colocalization of FLAG and GFP by pixel intensity-based assessment (n=28 nuclei).

B) Comparing the total amounts of chromatin-bound SMC-1 and REC-8. Gonads from worms expressing either SMC-1::3xFLAG and mEos::HIM-3 (labeled as "GFP" in the figure to illustrate acquisition in the green channel) or REC-8::3xFLAG and GFP::COSA-1 were spread together on the same slides, immuno-stained for HIM-3 and FLAG, and imaged together using the same conditions. GFP::COSA-1 and mEos::HIM-3 served as internal markers to identify the genotypes of the nuclei being imaged; for the example nuclei depicted, similarities and difference in fluorescence intensities for HIM-3 and FLAG signals are illustrated using the indicated color scheme (generated using the Fire LUT from ImageJ). Graph indicates the total FLAG fluorescence measured in ROIs surrounding individual nuclei in SUM intensity projections; each data point represents a single nucleus. For each genotype, 6 late pachytene nuclei each from 4 different gonads were assayed. All values obtained are displayed, with no normalization applied. The ratio of the average total fluorescence values is 1 REC-8::3xFLAG : 3.94 SMC-1::3xFLAG.

C) Inferred number of SMC-1 molecules in individual axis foci. The total fluorescence for SMC-1::HA, REC-8::GFP and COH-3/4 was measured in individual 800x800 nm ROIs surrounding individual foci in SUM intensity projections of fully-spread nuclei; each data point represents the total fluorescence of SMC-1::HA in a single focus. As indicated in the cropped image on the top, SMC-1 foci were categorized as: localizing with COH-3/4, but not REC-8 (blue, left in the graph), localizing with both COH-3/4 and REC-8 (red, middle in the graph), or localizing with REC-8, but not COH-3/4 (green, right). All values obtained are plotted in the graph on the bottom. The Y-axis (representing arbitrary fluorescence units) is normalized to the mean fluorescence of SMC-1 foci that only localize with a REC-8 focus, but not with a COH-3/4 focus; this value is set to 1, as we consider REC-8 foci to represent single cohesin complexes.

D) Sample images (top) and quantitative data (graph and table) for experiments measuring fluorescence intensities of individual foci in parallel for pairwise combinations of axis proteins. Nuclei from worms expressing 3xFLAG::HTP-3::GFP and nuclei from worms expressing REC-8::GFP, HTP-1::GFP or GFP::HIM-3 were spread together on the same slides, immuno-stained for GFP and FLAG, and imaged together using the same

conditions. Presence or absence of FLAG staining (blue in the sample images) was used to identify the genotype of the nuclei; asterisks indicate unspread nuclei of the same genotype that were present in the same field. Total fluorescence was measured in 400x400 nm ROIs surrounding well-separated individual foci in SUM intensity projections; each data point represents a single focus. Different pairwise data sets were normalized to each other using the mean fluorescence of HTP-3::GFP foci as a normalization standard. The Y-axis (representing arbitrary fluorescence units) is normalized to mean REC-8::GFP = 1, as we consider REC-8 foci to represent single molecules.

Figure 2S1. **Supporting evidence for quantification of cohesin molecules.** A) SIM images of partially-spread nuclei from a worm expressing both REC-8::GFP and REC-8::3xFLAG, immuno-stained for HTP-3, FLAG and GFP. TOP: All primary antibodies (anti-FLAG, ant-GFP and anti-HTP-3) were applied at the same time. Center panel was generated using ImageJ plugin "ColocThreshold", with white indicating the rare pixels with significant FLAG and GFP colocalization. BOTTOM: For the nucleus depicted, the specimen was stained sequentially: anti-FLAG was applied first, followed by secondary detection, before primary and secondary immuno-detection of HTP-3 and GFP (the opposite staining order was presented in FIG2A). Importantly, in all three orders in which the experiment was performed (sequential staining in both directions and simultaneous co-staining with all primary antibodies), GFP and FLAG both localize to chromosome axes (marked by HTP-3) in similar numbers, but they do not colocalize with each other, ruling out antibody exclusion artifacts.

B) COH-3/4 and SMC-1 fluorescence values correlate with each other in fully spread nuclei from worms expressing SMC-1::HA. LEFT: SIM image of well-spread chromosome segments in which relative intensities of immuno-fluorescence signals are depicted using the indicated color scale, illustrating the strong similarity between the fluorescence intensity patterns for COH-3/4 (top) and SMC-1::HA (bottom). RIGHT: Graph plotting fluorescence values for SMC-1::HA (x-axis) and COH-3/4 (Y-axis) in 800x800 nm ROIs centered on individual axis foci from SUM projected, wide-field images. R^2 value reflects a strong positive correlation between SMC-1 and COH-3/4 fluorescence values in individual foci.

Figure 2S2. **Assessment of relative levels of chromosome-associated HORMAD proteins in whole nuclei.** A) SUM-projected non-deconvolved wide field images (left) of leptotene nuclei from partially-spread gonads from 3xFLAG::HTP-3::GFP and GFP::HIM-3 expressing worms processed in parallel for immuno-fluorescence on the same slide. Each data point in the graph (right) represents the total fluorescence in a single nucleus.

B) Fully-spread nuclei from worms expressing 3xFLAG::HTP-3::GFP and from worms expressing HTP-1::GFP (either in the presence or absence of HTP-2) were prepared as in Figure 2D on the same slide (example image on the left). Nuclei were stained sequentially for GFP and COH-3/4, followed by detection of the FLAG epitope to identify the nuclei expressing 3xFLAG::HTP-3::GFP. Total immuno-fluorescence signals for GFP (green channel) and COH-3/4 (far-red channel) were measured in ROIs drawn around each individual nucleus. Each data point in the graph represents the ratio of total GFP signal : total COH-3/4 signal for a single nucleus (to account for differences in the degree of spreading of individual nuclei). Data for the two experiments were normalized to each other using the mean value for HTP-3::GFP as a normalization standard; HTP-3::GFP values for only one of the two experiments are presented in the graph.

C) SUM intensity projections of non-spread WT gonads stained for DAPI, HTP-3 and HTP-1/2, or DAPI, HTP-3 and HIM-3; the gonads were divided as depicted into nineteen equal-sized, half-overlapping ROIs from the mitotic tip to start of cellularization (late diplotene). For each HORMAD being evaluated (HTP-3, HIM-3 or HTP-1/2), the ratio of total immuno-fluorescence signal / total DAPI signal was determined for each ROI. For the plots of relative fluorescence (for each HORMAD) over the course of meiotic prophase progression, measured values were normalized to the average value for the set of ROIs spanning from the onset of meiotic prophase (ROI 6) through the end of the pachytene stage (ROI 16-17). Two gonads were averaged for each staining. Note that HTP-3 levels remain stable over the course of meiotic prophase, whereas HTP-1/2 and HIM-3 levels increase.

Figure 3. **Non-random distribution of functionally and structurally distinct cohesin complexes.**

A) Reduction in chromosome-associated REC-8 cohesion-conferring complexes occurs concurrently with axis formation. LEFT: Deconvolved wide-field images of a partially spread gonad from a worm expressing REC-8::GFP, stained for GFP, COH-3/4 and DNA, illustrating that COH-3/4 becomes detectable on chromatin at leptotene entry and REC-8 signal intensity drops concurrently. As nuclei in this region of the gonad move approximately one row every 40 minutes (Rosu and Cohen-Fix, 2017), the fact that nuclei with medium levels of COH-3/4 or REC-8) are rarely observed suggests that this is a rapid transition. RIGHT: Quantitation of total REC-8 or COH-3/4 fluorescence in nuclei at pre-leptotene and leptotene/zygotene stages, measured using SUM projections of 3D-stiched gonads. Each data point represents a single nucleus; for each of the 4 gonads analyzed for each kleisin, fluorescence levels were normalized to 100 for the mean fluorescence in pre-leptotene nuclei for REC-8 and for the mean fluorescence in leptotene/zygotene nuclei for COH-3/4. REC-8 fluorescence drops at leptotene entry to half its pre-leptotene levels. The images below the graph illustrate the drop in REC-8 using the indicated color scale to depict fluorescence signal intensity and boxes to indicate the regions of the gonad where fluorescence was quantified.

B) Non-random, alternating distribution of cohesin complexes containing different kleisin subunits along chromosome axes. TOP: SIM image of axis segments from a fully-spread prophase nucleus, illustrating lack of colocalization of COH-3/4 and REC-8. MIDDLE: Graphical representation of automated signal peak calling for a sample Z-projected straightened single axis, illustrating that the positions of REC-8 and COH-3/4 peaks usually do not coincide. Each line in the in the table below represents such a single, Z-projected and straightened axis segment, with R indicating REC-8 foci and C indicating COH-3/4 foci. Yellow indicates that both direct neighbors of a given kleisin focus are of the other kleisin type. Red (COH-3/4) or green (REC-8) indicates that the indicated focus has one like neighbor and one different neighbor. Darkening red or green represent more than two kleisins of the same kind in a row. Orange represents two, non-resolvable REC-8 and COH-3/4 signal peaks (such as the first signal peak in top, right). Axis segments are sorted by the number of cohesin foci (indicated at the

right); all analyzed segments are presented (n = 18 segments from 3 nuclei). REC-8 and COH-3/4 foci alternate with each other in a highly non-random fashion (*e.g.*: stretches of three or more of the same kleisin were observed much less frequently than expected for a random distribution (10 observed *vs.* 131 expected; $p<0.00001$, chi-square test, www.socscistatistics.com). BOTTOM: Example of simulated data obtained using 50% C and 50% R as input for https://www.random.org/lists.

C) Evidence for association of COH-3/4 cohesin complexes with individual chromatids. RIGHT TOP: SIM image of SYP-1, HTP-3 and COH-3/4 immuno-staining in three meiotic prophase nuclei from a *rec-8* mutant gonad; all three nuclei shown display a combination of SCs and unsynapsed chromosomes. MIDDLE: Tracings of individual SCs from the above nuclei; blue numbers indicate the total number of SCs in each nucleus. BOTTOM: Nuclei with SCs pseudo-colored in blue together with images of unsynapsed chromosome axes (marked with HTP-3 and COH-3/4); green numbers indicate the number of unsynapsed chromosome axes present in each individual nucleus. When unsynapsed chromosome stretches were detected in the *rec-8* mutant, they were consistently present in even numbers. Moreover, in nuclei where all SCs and unsynapsed axes could be reliably traced, we found that 2 x (the number of SCs) + (the number of unsynapsed axes) = 24, corresponding to the total number of chromatids present. Based on these numbers (and SC lengths measuring approximately 75-80% the lengths of normal SCs, see FIG3S1C), we infer that SCs form between sister chromatid pairs in the *rec-8* mutant and that unsynapsed chromosome stretches correspond to individual chromatids.

Figure 3S1. **Functional distinctions between REC-8 and COH-3/4 cohesin complexes.** A) SIM images of HORMAD proteins and REC-8 in partially spread meiotic prophase nuclei from the *coh-3 coh-4* mutant, illustrating the requirement for COH-3/4 in axis organization. HORMADs and REC-8 still bind to chromatin in this mutant, but the high degree of colocalization between HTP-3, HTP-1/2 and REC-8 seen in the WT is not observed and continuous axes do not form.

B) Reduction in chromosome-associated REC-8 cohesion-conferring complexes occurs independently of installation of COH-3/4 axis-organizing cohesins. Non-spread gonads

from WT, *coh-3/4* and *wapl-1* worms, with relative intensities of REC-8 immuno-fluorescence signals illustrated using the indicated color scale. The drop of REC-8 levels observed in the WT does not depend on the loading of COH-3/4, as it still occurs in their absence. However, a drop in REC-8 levels does not occur in the *wapl-1* mutant.

C) SIM images of individual chromosomes from partially-spread meiotic prophase nuclei prepared using conditions that preserve association of SC central region proteins and maintain inter-axis distances comparable to *in situ* preparations (Woglar and Villeneuve, 2018). Left, Representative example images of SCs in a WT pachytene nucleus, provided together with traces of the paths of individual SCs that were generated using the ImageJ plugin "Simple Neurite Tracer" (Longair et al., 2011), illustrating that the paths of all six individual synapsed chromosome pairs can be reliably traced in 3D using this approach. Right, Example images of SCs of straightened chromosomes, indicating the average lengths of wild-type early pachytene SCs (identified based on the presence of multiple recombination foci [marked by RPA and BLM] per SC), wild-type late pachytene SCs (which have a single bright COSA-1-marked crossover site focus per SC), and the inter-sister SCs that are formed in a *rec-8* mutant.

Figure 4. **Model for chromosome axis organization and evidence for asymmetry between sister chromatid loops**. A) LEFT: A quantitative model for chromosome axis module composition, stoichiometry, and density derived from the data presented here and in (Kim et al., 2014). RIGHT: Model of chromosome axis organization based on the data presented; see text for description.

B) Schemata explaining the experimental strategy for determining whether the chromosome loops that form on a pair of sister chromatids are "symmetric" (same size, same genomic position) or "asymmetric" (different sizes, different genomic position), by measuring the relative distances between a specific genomic position (on each chromatid) and the chromosome axis. The specific genomic position assayed is the junction point between two consecutive 200 kbp FISH probes on chromosome II (probe A1 targets II..11.5-11.7 Mbp ; probe A2 targets II..11.7-11.9).

C) Schematic illustrating the use of *mIn1*, a rearranged version of chromosome II harboring an 8.2 Mbp internal inversion, for assessment of sister chromatid loop

relationships. *mIn1* heterozygosity results in wide (>7Mbp) separation between the FISH signals for the normal and rearranged homologs, thereby enabling assessment of sister chromatid signals.

D) Immuno-FISH evidence for asymmetry between sister chromatid loops. Images shown are two examples of individually cropped heterozygous *mIn1* bivalents, immuno-stained for HTP-3 and hybridized with FISH probes A1 and A2. These examples illustrate the three categories of FISH signals scored; sister chromatid loops were scored as "asymmetric" when the distances (measured in 3D) from the two FISH probe junctions to the axis differed by greater than 400 nm. Graph on the right indicates the percent of FISH signals for each category. For this quantification, we analyzed all FISH signals localizing in the minimally disrupted, non-adhered portion of the nuclei of one gonad prepared using partially spreading conditions (see FIG4S1). For 8% (7/88) of these sites, an unambiguous meeting point of the two FISH probes could not be determined, either because the detection for one of the two probes failed or because signals for one probe were splintered (potentially due to preparation artifacts). The graph reports scoring for the remaining 81/88 sister pairs that could be analyzed.

Figure 4S1: **Adhered *vs.* non-adhered side in partially spread nuclei.** Illustration indicating which side of the nucleus was assayed to determine the distances between FISH signal junctions and the chromosome axis in FIG4D. The side of the nucleus that adheres to the glass (magenta frame, left) in the partial spreading procedure is visibly more flattened than the non-adhering side (green frame, right). Moreover, adherence of chromatin/DNA to the glass slide itself potentially introduces artifacts affecting DNA/chromatin organization. Therefore, only FISH signals that were associated with chromosome segments in the non-adhering side of the nucleus were assayed for FIG4D.

MATERIALS AND METHODS:

C. elegans culture conditions:

Worms were grown on *E. coli* (OP50) seeded NG agar plates at 20˚C according to the standard method (Stiernagle, 2006). For experiments, worms were either selected as

homozygous L4 larvae (from heterozygous strains maintained using balancer chromosomes) or were harvested as staged L1 larvae following bleaching of gravid adults (for strains maintained as homozygotes) according to: (Stiernagle, 2006) and were analyzed 24-36 hours post L4 stage. For experiments using two tagged versions of REC-8 (Fig 3A) ATGSi23 (*rec-8::GFP; rec-8 (null)*) hermaphrodites were mated with CA1481 (*rec-8::3xFLAG*) males, and leptotene/zygotene nuclei of F1 heterozygous hermaphrodites, which expressed both REC-8 tagged proteins (and no untagged REC-8), were analyzed 36 hours post L4 stage.

C. elegans strains used in this study:

- N2
- ATGSi23: *fqSi23[Prec-8::rec-8:::GFP::rec-8 3'UTR + cb-unc-119(+)] II; rec-8(ok978) IV*
- CA1481: *meIs8[Ppie-1::GFP::cosa-1 + cb-unc-119(+)] II; rec-8(ie35[rec-8::3xFLAG]) IV*
- TY4986: *htp-3(y428) ccIs4251 I/hT2 (I, III)*
- ATG98: *wapl-1(tm1814) IV/nt1[qIs51] (IV,V)*
- TY5120: *+/nT1 IV; coh-4(tm1857) coh-3(gk112) V/nT1[qIs51] (IV;V)*
- VC666: *rec-8(ok978) IV/nT1[qIs51] (IV;V)*
- AV1079: *meEx001; rec-8(ok978)/nT1[qIs51] (IV;V)*
- EG699: *ttTi5605 II; unc-119 (ed3); oxEx1578*
- CA1282: *him-3(ie114[gfp::him-3]) IV*
- CA1437: *htp-3(tm3655) I; ieSi62[Phtp-3::3×Flag::htp-3::GFP::htp-3 3'UTR + unc-119(+)] II; him-3(ie33[mEos2::him-3]) IV*
- ATGSi43: *fqSi37[htp-1::GFP cb-unc-119(+)] II; htp-1(gk174) IV*
- AV1080: *fqSi37[htp-1::GFP cb-unc-119(+)] II; htp-1(gk174) htp-2(tm2543) IV*
- AV1088: *smc-1(ie39[smc-1::intHA]) I; fqSi23[Prec-8::rec-8:::GFP::rec-8 3'UTR + cb-unc-119(+)] II; rec-8(ok978) IV*
- VC1474: *top-2(ok1930)/mIn1[mIs14 dpy-10(e128)]* II
- CA1432: *smc-1(ie36[smc-1::3xFlag]) I; meIs8[Ppie-1::GFP::cosa-1 + cb-unc-119(+)] II; him-3(ie33[mEos2::him-3]) IV*

Microinjection of *C. elegans*:

Microinjection was performed using a FemtoJet 4i injector system (Eppendorf) and an Axiovert 10 microscope (Zeiss). Injection mixes contained a total of 100ng DNA in distilled water. The injection mix for *meEx001* contained the dominant selection plasmids pGH8 (*prab-3::mCherry::unc-54_3'UTR,* 2.5ng) and pBR186 (modified from pDD282, includes *sqt-1p::sqt-1(e1350):: sqt-1_3'UTR _hsp16::Cre::tbb-2_3'UTR_rps-11p::HygR::unc-54_3'UTR,* 2.5ng) in addition to 95 ng *E. coli* (OP50) DNA, isolated by standard protocols, sonicated and size-selected for fragments of 1-5 kb by agarose gel purification.

Full spreading and staining of nuclei:

Worms were staged by bleaching, grown at 20˚C and harvested 24-36h post L4 stage (pelleted by gravitation), washed 3 times in 0.35x nuclear purification buffer (NPB; 3.5 mM HEPES pH 7.5, 14 mL NaCl, 31.5 mM KCl, 0.07 mM EDTA, 0.175 mM EGTA, 0.07 mM DTT, 0.035% Triton X-100). The resulting worm pellet was mixed with 1 volume 0.35x NBP and frozen as worm beads by dropping 50 µl drops of NBP-worm slurry into liquid nitrogen. 2-10 beads were ground for 10 seconds using a liquid nitrogen cooled mortar and pestle. The ground tissue was transferred into a 50 ml Falcon tube with a kitchen spoon, thawed and pipetted up and down several times to release nuclei. 5 µl of this suspension was applied on an EtOH-washed 22x40mm coverslip. 50µl of spreading solution (see below) was added and nuclei were immediately distributed over the whole coverslip using a pipette tip. Coverslips were left to dry at room temperature (approximately 1 hour) and post-dried for two more hours at 37°C, washed for 20 minutes in methanol at -20°C and rehydrated by washing 3 times for 5 minutes in PBS-T. A 20-minute blocking in 1% w/v BSA in PBS-T at room temperature was followed by overnight incubation with primary antibodies at 4°C (antibodies diluted in: 1% w/v BSA in PBS-T supplied with 0.05% w/v NaN_3). Coverslips were washed 3 times for 5 minutes in PBS-T before secondary antibody incubation for 2 hours at room temperature. After PBS-T washes, the nuclei were immersed in Vectashield (Vector) and the coverslip was mounted on a slide and sealed with nail polish. Spreading solution: (for one coverslip, 50µl): 32µl

of Fixative (4% w/v Paraformaldehyde and 3.2–3.6% w/v Sucrose in water), 16µl of Lipsol solution (1% v/v/ Lipsol in water), 2µl of Sarcosyl solution (1% w/v of Sarcosyl in water).

Partial spreading and staining of nuclei:

Partial spreading of *C. elegans* gonads was performed as in (Pattabiraman et al., 2017). The gonads of 20–100 adult worms were dissected in 5µl dissection solution (see below) on an EtOH-washed 22x40mm coverslip. 50µl of spreading solution (see above) was added and gonads were immediately distributed over the whole coverslip using a pipette tip. Coverslips were left to dry at room temperature (approximately 1 hour) and post-dried for two more hours at 37°C, washed for 20 minutes in methanol at -20°C and rehydrated by washing 3 times for 5 minutes in PBS-T. A 20-minute blocking in 1% w/v BSA in PBS-T at room temperature was followed by overnight incubation with primary antibodies at 4°C (antibodies diluted in: 1% w/v BSA in PBS-T supplied with 0.05% w/v NaN_3). Coverslips were washed 3 times for 5 minutes in PBS-T before secondary antibody incubation for 2 hours at room temperature. After PBS-T washes, the nuclei were immersed in Vectashield (Vector) and the coverslip was mounted on a slide and sealed with nail polish. Dissection solution: For Figures 1A, 1S1, 1S2A, 2S2A, 3B, 3S1A, 4D and 4S1 gonads were dissected in 10-30% v/v Hank's Balanced Salt Solution (HBSS, Life Technology, 24020-117) with 0.1% v/v Tween-20. For Figures 1S2B, 2S2C, 3C, 3S1B and 3S1D gonads were dissected in 50-85% v/v Hank's Balanced Salt Solution (HBSS, Life Technology, 24020-117) with 0.1% v/v Tween-20.

Antibodies used in this study:

The following primary antibodies used: Chicken anti-HTP-3 (1:500) (MacQueen et al., 2005), chicken anti-GFP (1:2000) (Abcam), mouse anti-GFP (1:500) (Roche), rabbit anti-GFP (1:500) (Yokoo et al., 2012), mouse anti-HA (1:1000) (Covance/Biolegend), guinea pig anti-SYP-1 (1:200) (MacQueen et al., 2002), mouse anti-H3K9me2 (1:500) (Abcam), rabbit anti-SMC-1 (1:200) (Chan et al., 2003), rabbit anti-COH-3/4 (1:5000) (Severson and Meyer, 2014), rabbit anti-REC-8 (1:10000) (Novus Biologicals), rabbit anti-HIM-3 (1:200) (Zetka et al., 1999), rabbit anti-HTP-1/2 (1:500) (Martinez-Perez et al., 2008) and mouse anti-FLAG (1:200) (Sigma).

Secondary antibodies conjugated to Alexa dyes 405, 488, 555 or 647, obtained from Molecular Probes, were used at 1:500 dilution (Alexa 488 and 555), 1:200 (Alexa 647) and 1:100 (Alexa 405). In cases where antibodies raised in mouse and guinea pig were used on the same sample, we used highly cross-absorbed goat anti-mouse secondary antibodies, obtained from Biotum (conjugated to CF488, or CF555 respectively) for secondary detection of the mouse primary antibody in order to avoid cross-reaction against antibodies raised in guinea pig.

Imaging:

Imaging, deconvolution and 3D-SIM reconstruction were performed as in (Pattabiraman et al., 2017). Wide field (WF) images were obtained as 200 nm spaced Z-stacks, using a 100x NA 1.40 objective on a DeltaVison OMX Blaze microscopy system, deconvolved and corrected for registration using SoftWoRx. Subsequently, gonads were assembled using the "Grid/Collection" plugin (Preibisch et al., 2009) in ImageJ. For display, pictures were projected using maximum intensity projection in ImageJ. 3D-Structured Illumination microscopy images were obtained as 125 nm spaced Z-stacks, using a 100x NA 1.40 objective on a DeltaVison OMX Blaze microscopy system, 3D-reconstructed and corrected for registration using SoftWoRx. For display, images were projected using maximum intensity projection in ImageJ or SoftWoRx. For display in figures, contrast and brightness were adjusted in individual color channels using ImageJ.

Manual quantification of axis foci:

Axis foci were counted manually on 32-bit Z-projected SIM images. For this analysis, foci are defined as fluorescence signals that 1) display individual maxima in non-overlapping ROIs $\geq$ 3x3 pixels in size and 2) were at least five times brighter than background average (with most ranging from 10-100 times brighter than background).

Quantitation of relative levels of chromosome axis proteins present in individual axis modules:

Nuclei from worms expressing 3xFLAG::HTP-3::GFP and nuclei from worms expressing REC-8::GFP, HTP-1::GFP or GFP::HIM-3 were isolated in parallel, mixed, and spread

together on the same slides. GFP was labeled using primary and secondary antibodies prior to primary and secondary detection of the FLAG epitope to identify the nuclei expressing 3xFLAG::HTP-3::GFP, and nuclei on the same slide were imaged in parallel using the same conditions. SUM intensity projections were generated from non-deconvolved 32-bit images, and total fluorescence was measured in 400x400 nm ROIs surrounding well-separated individual foci. Fluorescence measurements were made for 25-70 well-separated foci per nucleus (4-9 nuclei for each axis component); each data point represents a single focus. Different pairwise data sets were normalized to each other using the mean fluorescence of HTP-3::GFP foci as a normalization standard. The Y-axis (representing arbitrary fluorescence units) is normalized to mean REC-8::GFP = 1, as we consider REC-8 foci to represent single molecules.

Assessing localization of REC-8 and COH-3/4 on straightened axes:

Axis segments that did not twist around the homologous partner locally and were not spread on top of each other in maximum intensity Z-projected SIM images were manually traced and straightened using the ImageJ ‘’Segmented Line Tool” and “Selection straighten” operation as a 10 pixel-wide band. Signal peaks in individual channels were manually identified and marked as a single pixel along the band. The individual channels were analyzed separately, and the outputs were overlaid prior to manual readout of the spatial relationships of peak positions, resulting in the graphs presented in Figure 3.

Colocalization analysis using Coloc2:

Colocalization was assessed by evaluating the correlation of pixel intensities over space using the Coloc2 plugin of ImageJ. R values around 0 indicated lack of colocalization while an R value of 1 would indicate 100% colocation of signals in two channels, with their intensities completely correlated. 32-bit images were cropped and transformed into 8-bit single channels images. Background was subtracted in ImageJ using the sliding paraboloid background subtraction operation before running the Coloc2 analysis.

3D-tracing of chromosomes:

32-bit SIM images obtained from high salt spreads were transformed first into RBG color images and then into monochrome 8-bit images. In such images, individual chromosomes were traced using the "Simple Neurite Tracer" plug-in of ImageJ (Longair et al., 2011). For display and straightening of individual chromosomes, each individual chromosome path was exported as an 8-bit two-color mask with the "Fill Out" function of the "Simple Neurite Tracer". This mask was used to crop the individual chromosome in 3D from an RGB stack. These pictures were projected in Z and straightened using ImageJ ''Segmented Line Tool" and the "Selection straighten" operation.

Immuno-FISH and probe generation:

The oligopaint library was designed, FISH probes were generated and primary hybridization was performed as in (Mateo et al., 2019). After post-fixation, the sample was blocked in 1% w/v BSA in PBS-T at room temperature and further incubated overnight with primary antibodies at room temperature (antibodies diluted in: 1 % w/v BSA in PBS-T supplied with 0.05% w/v NaN_3). Coverslips washed 3 times for 5 minutes in PBS-T and blocked again in 1% w/v BSA in PBS-T. Coverslips were incubated with secondary antibodies for 2 hours at room temperature, and subsequently washed 3 times for 5 minutes in PBS-T. After the PBS-T washes, the coverslips were incubated with a secondary probe solution for 15 minutes. This solution consisted of: 50-nt complementary 'readout' oligos (0.1 nM) bound to a either a 20-nt Cy5-labeled or Cy3-labeled 'imaging' oligo (Cy5-5p-TGGGACGGTTCCAATCGGATC or Cy3-5p-ACCTCCGTTAGACCCGTCAG (0.12 nM)) in 25% ethylene carbonate and 2X SSC buffer. In order to label 200 Kb, the 'adaptor 1 readout' oligos 1-20, and 'adaptor 2 readout' oligos 21-40 were respectively pooled and labeled with either the Cy3 or Cy5-marked 'imaging' oligos. Coverslips were washed with 30% formamide in 2X SSC for two minutes, before 3 washes for 2 minutes each in 2X SSC. Finally, coverslips were mounted in Vectashield with DAPI.

REFERENCES:

Anderson, L.K., Stack, S.M., and Sherman, J.D. (1988). Spreading synaptonemal complexes from Zea mays. I. No synaptic adjustment of inversion loops during pachytene. Chromosoma *96*, 295-305.

Blat, Y., Protacio, R.U., Hunter, N., and Kleckner, N. (2002). Physical and functional interactions among basic chromosome organizational features govern early steps of meiotic chiasma formation. Cell *111*, 791-802.

Cattoglio, C., Pustova, I., Walther, N., Ho, J.J., Hantsche-Grininger, M., Inouye, C.J., Hossain, M.J., Dailey, G.M., Ellenberg, J., Darzacq, X.*, et al.* (2019). Determining cellular CTCF and cohesin abundances to constrain 3D genome models. eLife *8*.

Chan, R.C., Chan, A., Jeon, M., Wu, T.F., Pasqualone, D., Rougvie, A.E., and Meyer, B.J. (2003). Chromosome cohesion is regulated by a clock gene paralogue TIM-1. Nature *423*, 1002-1009.

Couteau, F., and Zetka, M. (2005). HTP-1 coordinates synaptonemal complex assembly with homolog alignment during meiosis in C. elegans. Genes & development *19*, 2744-2756.

Crawley, O., Barroso, C., Testori, S., Ferrandiz, N., Silva, N., Castellano-Pozo, M., Jaso-Tamame, A.L., and Martinez-Perez, E. (2016). Cohesin-interacting protein WAPL-1 regulates meiotic chromosome structure and cohesion by antagonizing specific cohesin complexes. eLife *5*, e10851.

Eijpe, M., Heyting, C., Gross, B., and Jessberger, R. (2000). Association of mammalian SMC1 and SMC3 proteins with meiotic chromosomes and synaptonemal complexes. Journal of cell science *113 (Pt 4)*, 673-682.

Eijpe, M., Offenberg, H., Jessberger, R., Revenkova, E., and Heyting, C. (2003). Meiotic cohesin REC8 marks the axial elements of rat synaptonemal complexes before cohesins SMC1beta and SMC3. The Journal of cell biology *160*, 657-670.

Frokjaer-Jensen, C., Davis, M.W., Ailion, M., and Jorgensen, E.M. (2012). Improved Mos1-mediated transgenesis in C. elegans. Nature methods *9*, 117-118.

Goodyer, W., Kaitna, S., Couteau, F., Ward, J.D., Boulton, S.J., and Zetka, M. (2008). HTP-3 links DSB formation with homolog pairing and crossing over during C. elegans meiosis. Developmental cell *14*, 263-274.

Gyuricza, M.R., Manheimer, K.B., Apte, V., Krishnan, B., Joyce, E.F., McKee, B.D., and McKim, K.S. (2016). Dynamic and Stable Cohesins Regulate Synaptonemal Complex Assembly and Chromosome Segregation. Current biology : CB *26*, 1688-1698.

Haber, J.E., Thorburn, P.C., and Rogers, D. (1984). Meiotic and mitotic behavior of dicentric chromosomes in Saccharomyces cerevisiae. Genetics *106*, 185-205.

Hollingsworth, N.M., and Byers, B. (1989). HOP1: a yeast meiotic pairing gene. Genetics *121*, 445-462.

Holzmann, J., Politi, A.Z., Nagasaka, K., Hantsche-Grininger, M., Walther, N., Koch, B., Fuchs, J., Durnberger, G., Tang, W., Ladurner, R.*, et al.* (2019). Absolute quantification of cohesin, CTCF and their regulators in human cells. eLife *8*.

Ishiguro, K., Kim, J., Fujiyama-Nakamura, S., Kato, S., and Watanabe, Y. (2011). A new meiosis-specific cohesin complex implicated in the cohesin code for homologous pairing. EMBO reports *12*, 267-275.

Ishiguro, K.I. (2019). The cohesin complex in mammalian meiosis. Genes to cells : devoted to molecular & cellular mechanisms *24*, 6-30.

Jackson, J.A., and Fink, G.R. (1985). Meiotic recombination between duplicated genetic elements in Saccharomyces cerevisiae. Genetics *109*, 303-332.

Kelly, W.G., Xu, S., Montgomery, M.K., and Fire, A. (1997). Distinct requirements for somatic and germline expression of a generally expressed Caernorhabditis elegans gene. Genetics *146*, 227-238.

Kim, K.P., Weiner, B.M., Zhang, L., Jordan, A., Dekker, J., and Kleckner, N. (2010). Sister cohesion and structural axis components mediate homolog bias of meiotic recombination. Cell *143*, 924-937.

Kim, Y., Rosenberg, S.C., Kugel, C.L., Kostow, N., Rog, O., Davydov, V., Su, T.Y., Dernburg, A.F., and Corbett, K.D. (2014). The chromosome axis controls meiotic events through a hierarchical assembly of HORMA domain proteins. Developmental cell *31*, 487-502.

Klein, F., Mahr, P., Galova, M., Buonomo, S.B., Michaelis, C., Nairz, K., and Nasmyth, K. (1999). A central role for cohesins in sister chromatid cohesion, formation of axial elements, and recombination during yeast meiosis. Cell *98*, 91-103.

Kohler, S., Wojcik, M., Xu, K., and Dernburg, A.F. (2017). Superresolution microscopy reveals the three-dimensional organization of meiotic chromosome axes in intact Caenorhabditis elegans tissue. Proceedings of the National Academy of Sciences of the United States of America *114*, E4734-E4743.

Longair, M.H., Baker, D.A., and Armstrong, J.D. (2011). Simple Neurite Tracer: open source software for reconstruction, visualization and analysis of neuronal processes. Bioinformatics *27*, 2453-2454.

MacQueen, A.J., Colaiacovo, M.P., McDonald, K., and Villeneuve, A.M. (2002). Synapsis-dependent and -independent mechanisms stabilize homolog pairing during meiotic prophase in C. elegans. Genes & development *16*, 2428-2442.

MacQueen, A.J., Phillips, C.M., Bhalla, N., Weiser, P., Villeneuve, A.M., and Dernburg, A.F. (2005). Chromosome sites play dual roles to establish homologous synapsis during meiosis in C. elegans. Cell *123*, 1037-1050.

Martinez-Perez, E., Schvarzstein, M., Barroso, C., Lightfoot, J., Dernburg, A.F., and Villeneuve, A.M. (2008). Crossovers trigger a remodeling of meiotic chromosome axis composition that is linked to two-step loss of sister chromatid cohesion. Genes & development *22*, 2886-2901.

Martinez-Perez, E., and Villeneuve, A.M. (2005). HTP-1-dependent constraints coordinate homolog pairing and synapsis and promote chiasma formation during C. elegans meiosis. Genes & development *19*, 2727-2743.

Mateo, L.J., Murphy, S.E., Hafner, A., Cinquini, I.S., Walker, C.A., and Boettiger, A.N. (2019). Visualizing DNA folding and RNA in embryos at single-cell resolution. Nature *568*, 49-54.

Mello, C.C., Kramer, J.M., Stinchcomb, D., and Ambros, V. (1991). Efficient gene transfer in C.elegans: extrachromosomal maintenance and integration of transforming sequences. The EMBO journal *10*, 3959-3970.

Miyoshi, T., Ito, M., Kugou, K., Yamada, S., Furuichi, M., Oda, A., Yamada, T., Hirota, K., Masai, H., and Ohta, K. (2012). A central coupler for recombination initiation linking chromosome architecture to S phase checkpoint. Molecular cell *47*, 722-733.

Panizza, S., Mendoza, M.A., Berlinger, M., Huang, L., Nicolas, A., Shirahige, K., and Klein, F. (2011). Spo11-accessory proteins link double-strand break sites to the chromosome axis in early meiotic recombination. Cell *146*, 372-383.

Parisi, S., McKay, M.J., Molnar, M., Thompson, M.A., van der Spek, P.J., van Drunen-Schoenmaker, E., Kanaar, R., Lehmann, E., Hoeijmakers, J.H., and Kohli, J. (1999). Rec8p, a meiotic recombination and sister chromatid cohesion phosphoprotein of the Rad21p family conserved from fission yeast to humans. Molecular and cellular biology *19*, 3515-3528.

Pasierbek, P., Jantsch, M., Melcher, M., Schleiffer, A., Schweizer, D., and Loidl, J. (2001). A Caenorhabditis elegans cohesion protein with functions in meiotic chromosome pairing and disjunction. Genes & development *15*, 1349-1360.

Patel, L., Kang, R., Rosenberg, S.C., Qiu, Y., Raviram, R., Chee, S., Hu, R., Ren, B., Cole, F., and Corbett, K.D. (2019). Dynamic reorganization of the genome shapes the recombination landscape in meiotic prophase. Nature structural & molecular biology *26*, 164-174.

Pattabiraman, D., Roelens, B., Woglar, A., and Villeneuve, A.M. (2017). Meiotic recombination modulates the structure and dynamics of the synaptonemal complex during C. elegans meiosis. PLoS genetics *13*, e1006670.

Preibisch, S., Saalfeld, S., and Tomancak, P. (2009). Globally optimal stitching of tiled 3D microscopic image acquisitions. Bioinformatics *25*, 1463-1465.

Rankin, S., and Dawson, D.S. (2016). Recent advances in cohesin biology. F1000Research *5*.

Rosenberg, S.C., and Corbett, K.D. (2015). The multifaceted roles of the HORMA domain in cellular signaling. The Journal of cell biology *211*, 745-755.

Rosu, S., and Cohen-Fix, O. (2017). Live-imaging analysis of germ cell proliferation in the C. elegans adult supports a stochastic model for stem cell proliferation. Developmental biology *423*, 93-100.

Schalk, J.A., Dietrich, A.J., Vink, A.C., Offenberg, H.H., van Aalderen, M., and Heyting, C. (1998). Localization of SCP2 and SCP3 protein molecules within synaptonemal complexes of the rat. Chromosoma *107*, 540-548.

Schwacha, A., and Kleckner, N. (1994). Identification of joint molecules that form frequently between homologs but rarely between sister chromatids during yeast meiosis. Cell *76*, 51-63.

Severson, A.F., Ling, L., van Zuylen, V., and Meyer, B.J. (2009). The axial element protein HTP-3 promotes cohesin loading and meiotic axis assembly in C. elegans to implement the meiotic program of chromosome segregation. Genes & development *23*, 1763-1778.

Severson, A.F., and Meyer, B.J. (2014). Divergent kleisin subunits of cohesin specify mechanisms to tether and release meiotic chromosomes. eLife *3*, e03467.

Smith, A.V., and Roeder, G.S. (1997). The yeast Red1 protein localizes to the cores of meiotic chromosomes. The Journal of cell biology *136*, 957-967.

Stiernagle, T. (2006). Maintenance of C. elegans. WormBook : the online review of C. elegans biology, 1-11.

Stinchcomb, D.T., Shaw, J.E., Carr, S.H., and Hirsh, D. (1985). Extrachromosomal DNA transformation of Caenorhabditis elegans. Molecular and cellular biology *5*, 3484-3496.

West, A.M., Rosenberg, S.C., Ur, S.N., Lehmer, M.K., Ye, Q., Hagemann, G., Caballero, I., Uson, I., MacQueen, A.J., Herzog, F.*, et al.* (2019). A conserved filamentous assembly underlies the structure of the meiotic chromosome axis. eLife *8*.

Woglar, A., and Villeneuve, A.M. (2018). Dynamic Architecture of DNA Repair Complexes and the Synaptonemal Complex at Sites of Meiotic Recombination. Cell *173*, 1678-1691 e1616.

Wojtasz, L., Daniel, K., Roig, I., Bolcun-Filas, E., Xu, H., Boonsanay, V., Eckmann, C.R., Cooke, H.J., Jasin, M., Keeney, S.*, et al.* (2009). Mouse HORMAD1 and HORMAD2, two conserved meiotic chromosomal proteins, are depleted from synapsed chromosome axes with the help of TRIP13 AAA-ATPase. PLoS genetics *5*, e1000702.

Woltering, D., Baumgartner, B., Bagchi, S., Larkin, B., Loidl, J., de los Santos, T., and Hollingsworth, N.M. (2000). Meiotic segregation, synapsis, and recombination checkpoint functions require physical interaction between the chromosomal proteins Red1p and Hop1p. Molecular and cellular biology *20*, 6646-6658.

Xu, H., Beasley, M.D., Warren, W.D., van der Horst, G.T., and McKay, M.J. (2005). Absence of mouse REC8 cohesin promotes synapsis of sister chromatids in meiosis. Developmental cell *8*, 949-961.

Yokoo, R., Zawadzki, K.A., Nabeshima, K., Drake, M., Arur, S., and Villeneuve, A.M. (2012). COSA-1 reveals robust homeostasis and separable licensing and reinforcement steps governing meiotic crossovers. Cell *149*, 75-87.

Zetka, M.C., Kawasaki, I., Strome, S., and Muller, F. (1999). Synapsis and chiasma formation in Caenorhabditis elegans require HIM-3, a meiotic chromosome core component that functions in chromosome segregation. Genes & development *13*, 2258-2270.

Zickler, D., and Kleckner, N. (2015). Recombination, Pairing, and Synapsis of Homologs during Meiosis. Cold Spring Harbor perspectives in biology *7*.

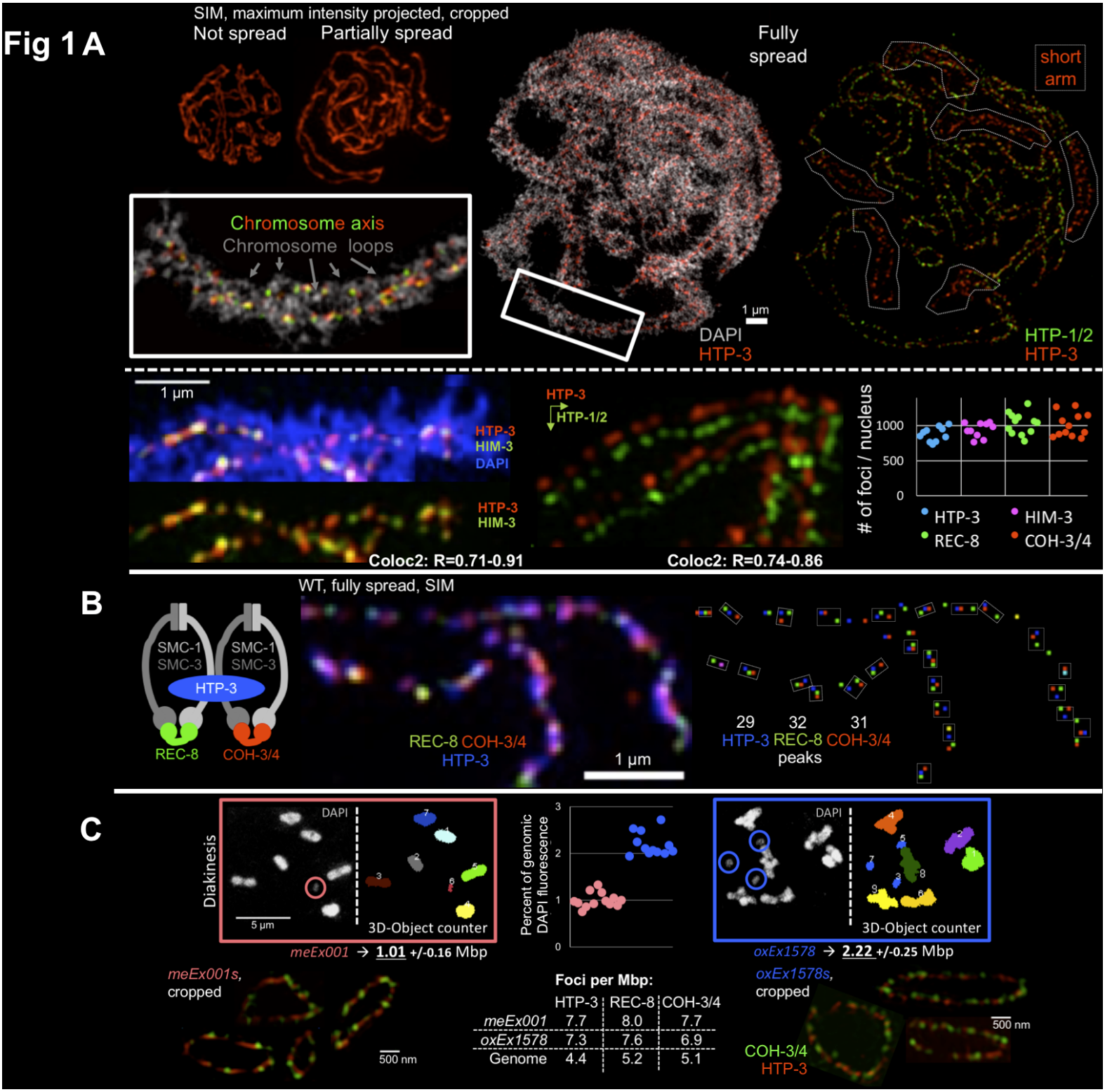

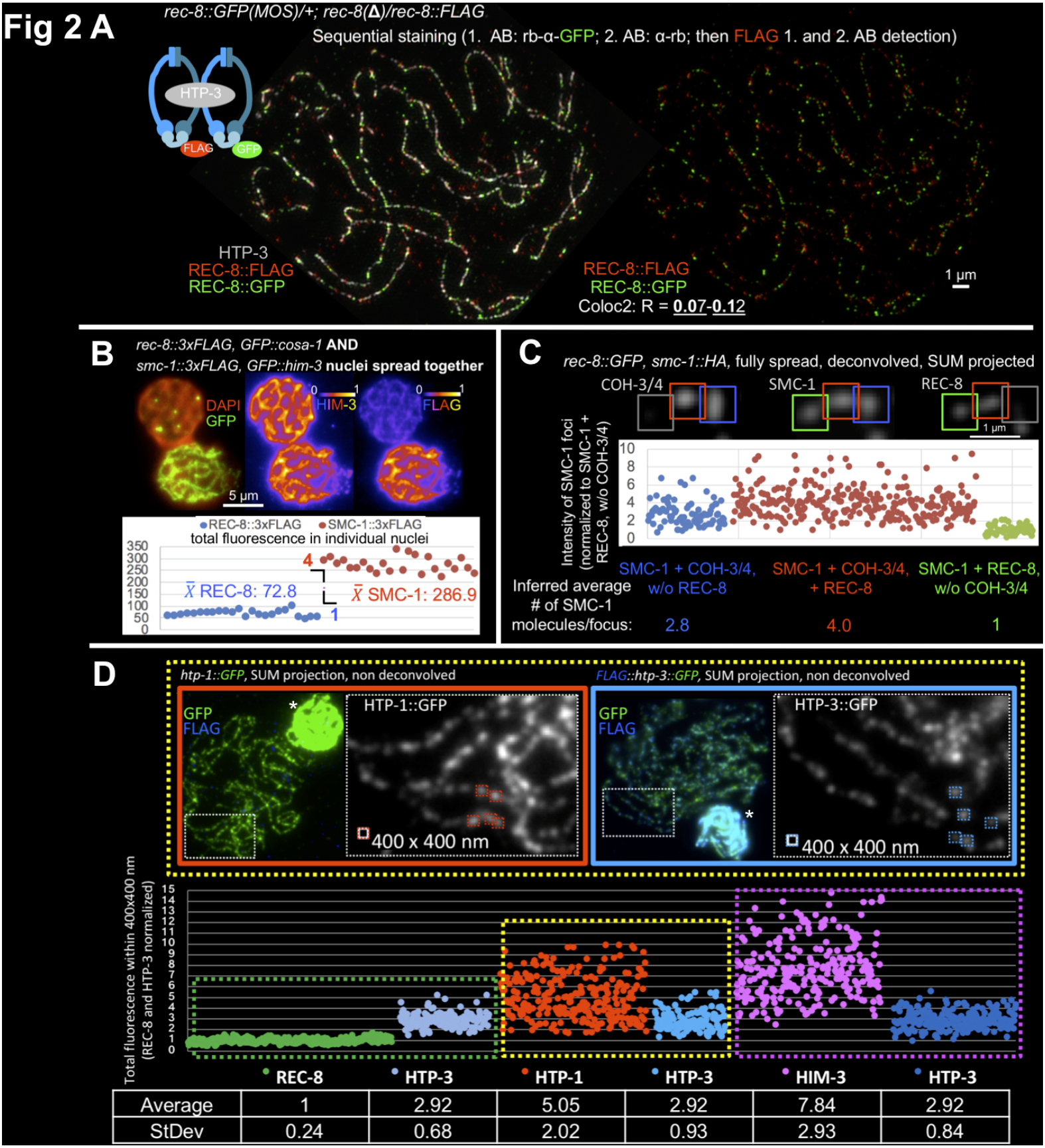

Average	1	2.92	5.05	2.92	7.84	2.92
StDev	0.24	0.68	2.02	0.93	2.93	0.84

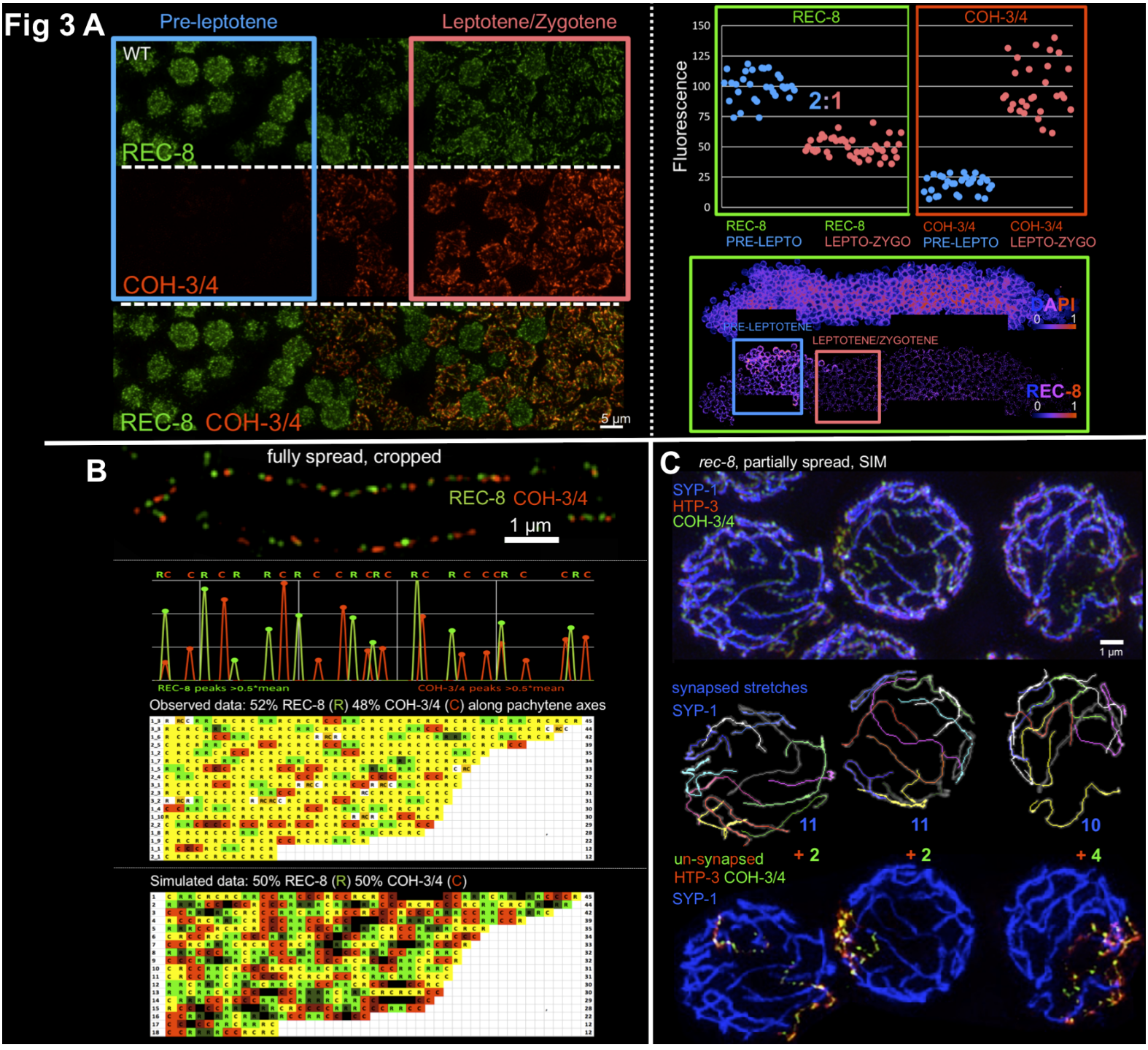

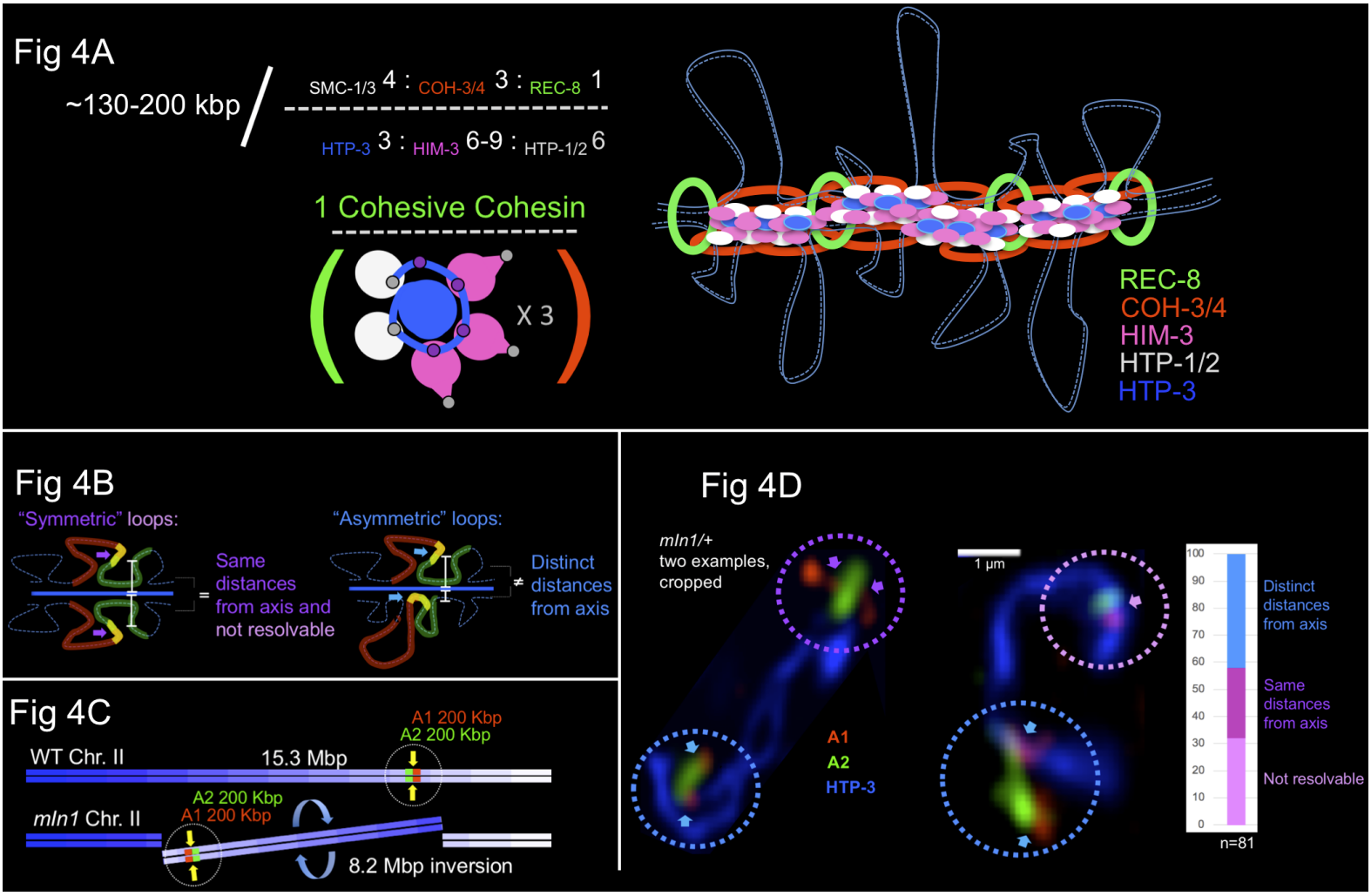

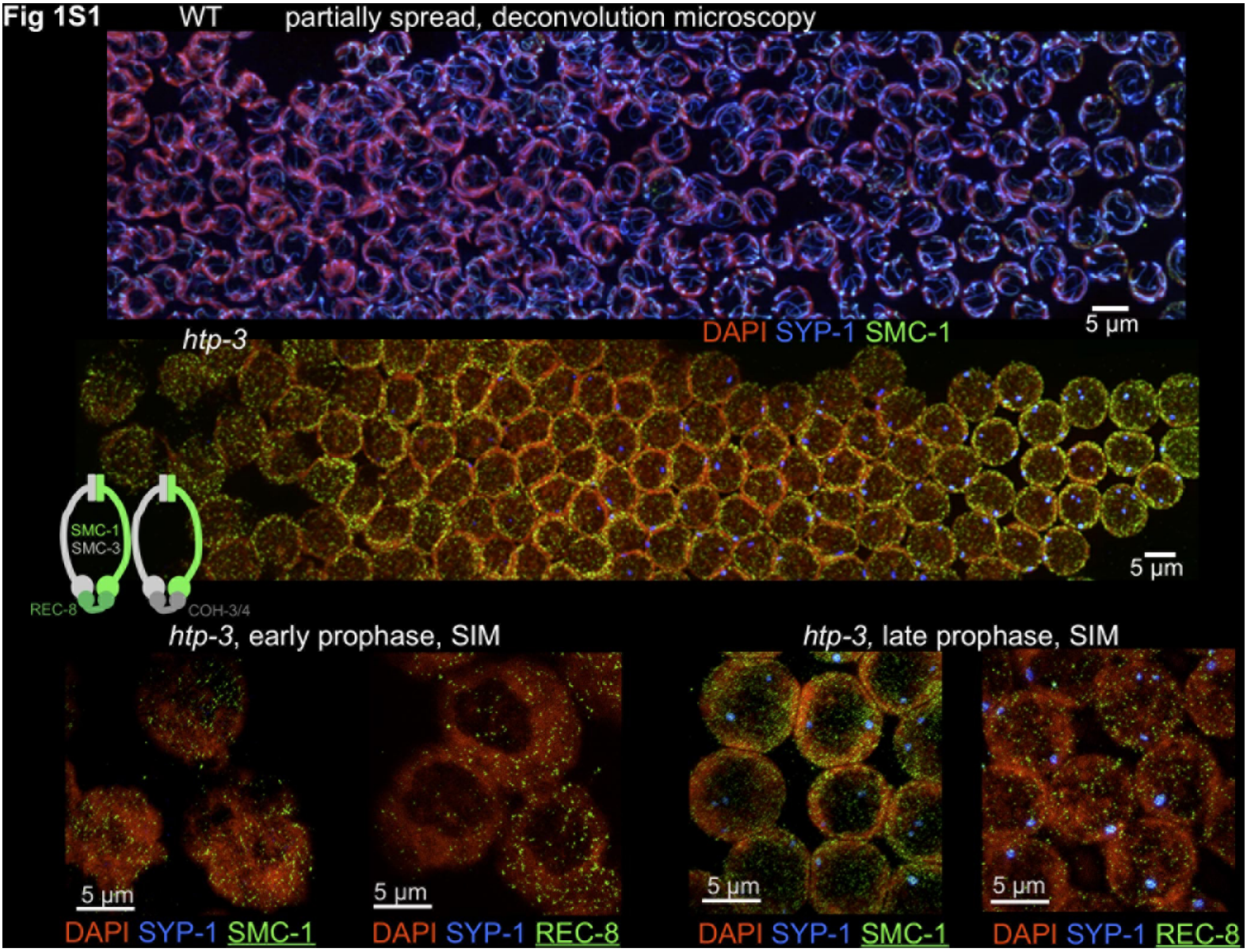

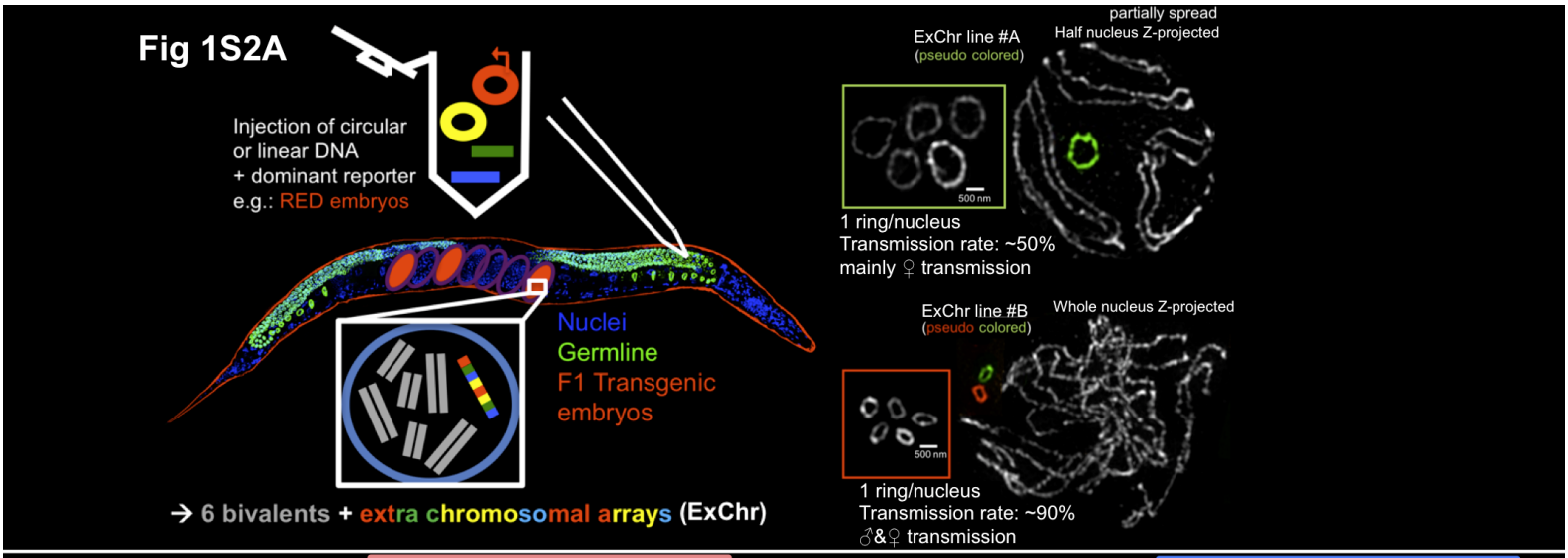

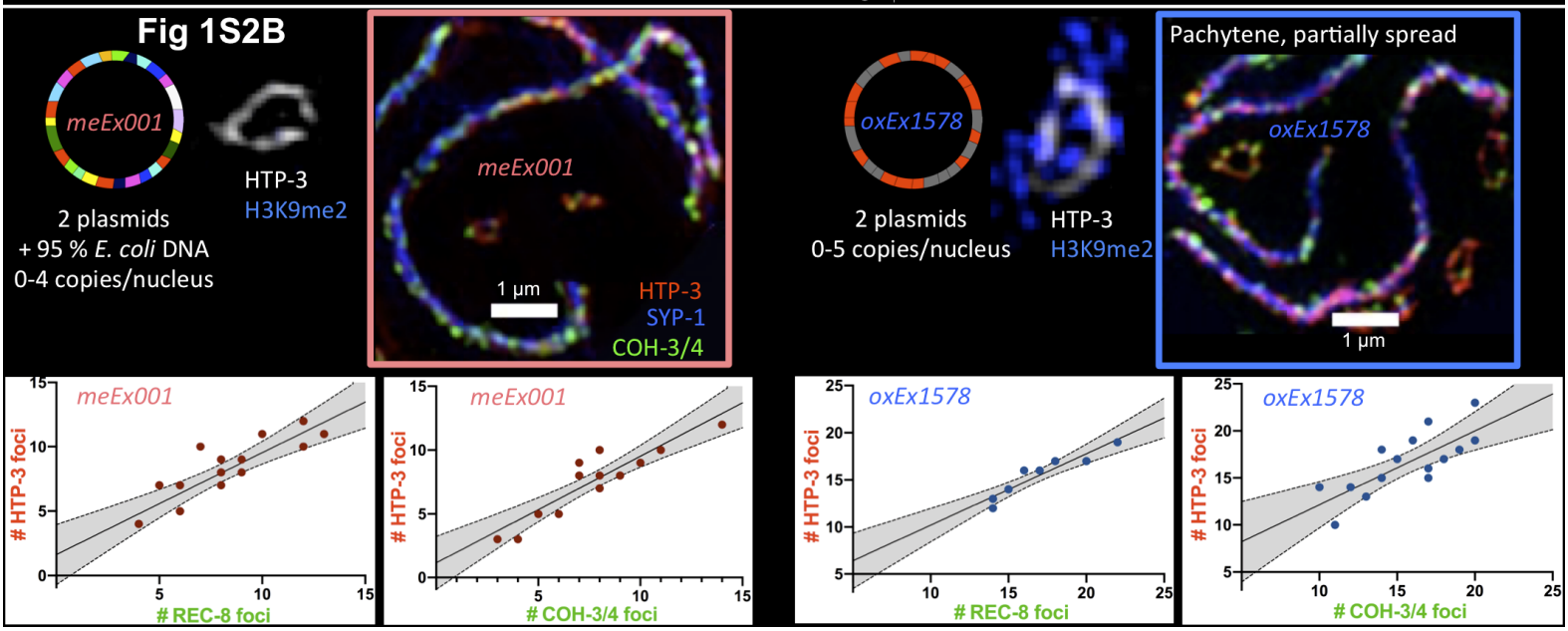

Fig 2S1 A

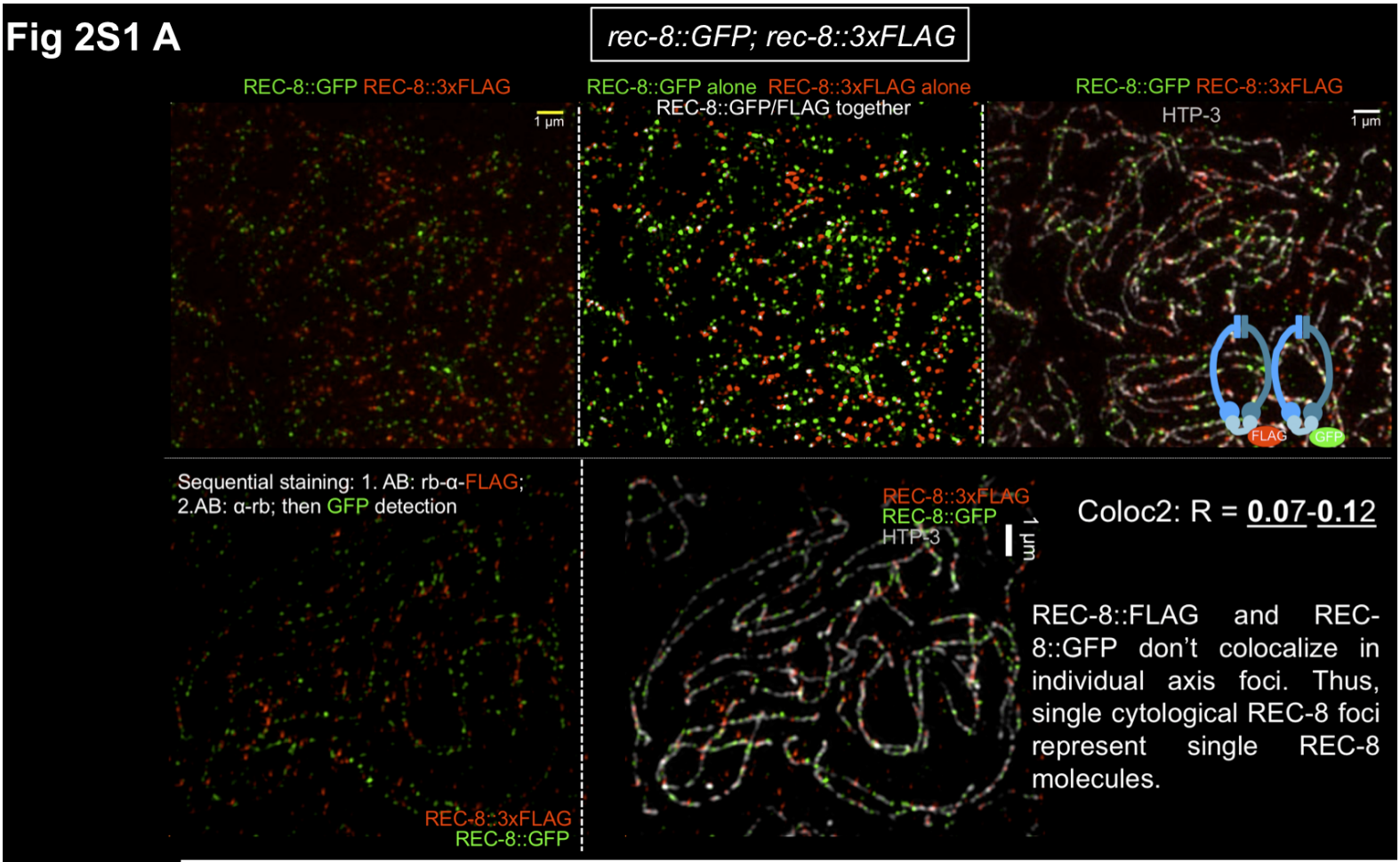

Fig 2S1 B